Title: An immunohistochemical atlas of necroptotic pathway expression

One Sentence Summary: Here we provide robust methodology to pinpoint necroptotic cell death pathway expression and activation in formalin-fixed mouse and human tissues.

Authors: Shené Chiou[1,2,^], Aysha H. Al-Ani[1,2,3,^], Yi Pan[1], Komal M. Patel[1], Isabel Y. Kong[4], Lachlan W. Whitehead[1,2], Amanda Light[1], Samuel N. Young[1], Marilou Barrios[1,2], Callum Sargeant[1,2], Pradeep Rajasekhar[1,2], Leah Zhu[1], Anne Hempel[1], Ann Lin[1], James A. Rickard[1,6], Cathrine Hall[1], Pradnya Gangatirkar[1], Raymond K.H. Yip[1,2], Wayne Cawthorne[1,2], Annette V. Jacobsen[1,2], Christopher R. Horne[1,2], Lisa J. Ioannidis[1,2], Diana S. Hansen[1,2,5], Jessica Day[1,2,3], Ian P. Wicks[1,2], Charity Law[1,2], Matthew E. Ritchie[1,2], Rory Bowden[1,2], Joanne M. Hildebrand[1,2], Lorraine A. O'Reilly[1,2], John Silke[1,2], Lisa Giulino-Roth[4], Ellen Tsui[1], Kelly L. Rogers[1,2], Edwin D. Hawkins[1,2], Britt Christensen[1,2,3], James M. Murphy[1,2,7,]* and André L. Samson[1,2,]*.

Affiliations: [1]Walter and Eliza Hall Institute of Medical Research, Parkville, Australia

[2]University of Melbourne, Parkville, Australia

[3]Royal Melbourne Hospital, Parkville, Australia

[4]Pediatric Hematology/Oncology, Weill Cornell Medical College, New York, USA

[5]Monash Biomedicine Discovery Institute, Department of Microbiology, Monash University, Clayton, Australia

[6]Austin Hospital, Heidelberg, Australia

[7]Drug Discovery Biology, Monash Institute of Pharmaceutical Sciences, Parkville, Australia

[^]These authors contributed equally to this work

*Joint senior and corresponding authors: jamesm@wehi.edu.au (JMM) and samson.a@wehi.edu.au (ALS).

Abstract: Necroptosis is a lytic form of regulated cell death reported to contribute to inflammatory diseases of the gut, skin and lung, as well as ischemic-reperfusion injuries of the kidney, heart and brain. However, precise identification of the cells and tissues that undergo necroptotic cell death *in vivo* has proven challenging in the absence of robust reagents and protocols for immunohistochemical detection. Here, we provide automated immunohistochemistry protocols to detect core necroptosis regulators – Caspase-8, RIPK1, RIPK3 and MLKL – in formalin-fixed mouse and human tissues. We observed surprising heterogeneity in protein expression within tissues, whereby short-lived immune barrier cells were replete with necroptotic effectors, whereas long-lived cells exhibited reduced RIPK3 or MLKL expression. Local changes in the expression of necroptotic effectors were observed in response to insults such as sterile inflammation, dysbiosis or immune challenge, consistent with necroptosis being dysregulated in disease contexts. This toolbox and methods will facilitate precise localisation and evaluation of necroptotic signaling *in vivo*.

Main text:

Introduction

The necroptotic cell death pathway leads to cell lysis and expulsion of cellular contents into the extracellular milieu, which in turn provokes an innate immune response. Necroptosis is considered to be an altruistic cell death pathway whose principal role is to protect the host from pathogens (*1-8*). Despite this, it is the aberrant functions of necroptosis associated with inflammatory diseases that have spurred interest in its underlying mechanisms and therapeutic prospects (*9, 10*). Studies of mice lacking the terminal effectors of the pathway – RIPK3 (Receptor-interacting protein kinase-3) or MLKL (Mixed-lineage kinase domain-like) – have led to the concept that excess necroptosis drives a range of inflammatory pathologies in organs including the skin, gut, brain, heart, lung, kidney and testes (*11-18*). However, many of these attributions have been disputed (*19-21*), likely reflecting an evolving understanding of the pathway and the limited availability of validated reagents to interrogate necroptosis in pathological specimens.

The core signaling axis of the necroptotic pathway has been well-defined and can be activated in response to a variety of inflammatory cues including ligation of Death, Toll-like or Pathogen-Pattern receptors (*22-28*). Caspase-8 is a critical negatively regulator of necroptotic signaling (*28*), whereby its deletion or loss-of-function promotes oligomerisation of RIPK1 (Receptor-interactor protein kinase-1), TRIF (TIR domain-containing adapter molecule 1) and/or ZBP1 (Z-DNA-binding protein 1) (*27*). This oligomeric structure, otherwise known as the necrosome, promotes activation of the downstream effectors RIPK3 and MLKL (*29*). RIPK3 recruits the MLKL pseudokinase to the necrosome, where it phosphorylates MLKL to provoke a conformational change, release from the necrosome, oligomerization and trafficking to the plasma membrane (*30-35*). At the plasma membrane, accumulation of activated MLKL to a critical threshold level is required for membrane permeabilization via a poorly understood mechanism that brings about the cell's demise (*33, 36, 37*).

As our understanding of the necroptosis pathway has grown, new tools and protocols have been developed to study necroptotic signaling in fixed cultured cells (*35, 38-40*). However, robust procedures for assessing the necroptotic pathway in tissues are still lacking, often leading to contradictory reports in the literature and misattributions of necroptotic pathologies. Here, we report automated immunostaining protocols for detecting Caspase-8, RIPK1, RIPK3 and MLKL, in mouse formalin-fixed paraffin-embedded tissues. These procedures have allowed assembly of an atlas of necroptotic pathway expression in mouse tissues under basal conditions and during innate immune challenge. While the necroptosis machinery is rarely expressed in cell types other than short-lived barrier cells in mouse tissues, sterile inflammation increased RIPK3 expression in the gut and liver, broadly predisposing multiple cell types to necroptotic death. In contrast, elimination of the intestinal microflora diminished RIPK3 expression and reduced necroptotic susceptibility. RIPK3 is also uniquely upregulated in splenic germinal centres and may influence antigen-specific immune responses in a non-necroptotic manner. Furthermore, we present robust protocols for detecting human Caspase-8, RIPK1 and MLKL and illustrate their utility for detecting dysregulated necroptosis in biopsies from patients with inflammatory bowel disease (IBD). Collectively, these protocols will empower the definitive evaluation of where and when necroptosis occurs in vivo in health and disease.

Results

Standardised immunohistochemical detection of the necroptotic pathway in mouse tissues

We recently compiled a toolbox of immunofluorescence assays to detect necroptotic signaling in cells (*38*). This toolbox requires use of: 1) non-crosslinking fixatives and 2) gene knockouts to account for non-specific signals; requirements that often cannot be met when immunostaining tissues. Here we aimed to develop robust immunohistochemistry protocols to detect the necroptotic pathway in formalin-fixed paraffin-embedded mouse tissues. Embedding and immunostaining was performed in an automated manner (see *Methods*) to allow reliable and scalable detection of the necroptotic pathway, and to lessen the future need to account for non-specific immunosignals using appropriate gene knockout controls. The specificity of thirteen monoclonal antibodies against Caspase-8, RIPK1, RIPK3 or MLKL was first tested by immunoblotting spleen homogenates from wild-type versus knockout mice (**Fig. S1**). The intensity and specificity of antibodies for immunohistochemistry was then iteratively optimised across 21 conditions (see *Methods* and **Fig. S1**). At each optimisation step, immunohistochemistry signals from the spleen of wild-type versus knockout mice were quantified (**Fig. 1Ai**), ratioed (**Fig. 1Aii**) and integrated to yield an index of performance (**Fig. 1Aiii**). For example, this pipeline improved the detection of RIPK1 with the monoclonal antibody D94C12 by approximately three orders of magnitude (**Fig. S1**). In total, seven automated immunohistochemistry protocols to detect mouse Caspase-8, RIPK1, RIPK3 or MLKL were developed (**Fig. 1B**). The detection of Caspase-8, RIPK1 and RIPK3 using these immunohistochemistry protocols (**Fig. 1B**) closely aligned with the abundance of these proteins across multiple tissues as measured by high-resolution quantitative mass spectrometry (**Fig. 1C**), indicating both specificity and sensitivity. Despite many rounds of optimisation with three specific anti-MLKL antibodies, mouse MLKL remained difficult to detect via immunohistochemistry in all tissues except spleen (**Fig. 1B,D** and **Fig. S1**).

Basal expression of the necroptotic pathway is restricted to fast-cycling immune barriers.

The immunohistochemical profile of Caspase-8, RIPK1, RIPK3 and MLKL across seven different organs suggested that expression of the necroptotic pathway is heavily restricted in unchallenged mice (**Fig. 1D**). For example, RIPK3$^+$ cells were scarce in the kidney and heart, and RIPK3 was undetectable in the brain (**Fig. 1D**). By comparison, co-expression of Caspase-8, RIPK1 and RIPK3 was evident in intestinal epithelial cells, some splenic regions and Kupffer cells (**Fig. 2A**). The *Tabula Muris* single cell RNA sequencing dataset supports the conclusion that expression of the necroptotic pathway is highly restricted in mice (**Fig. S2A**). Expression of the necroptotic effectors, MLKL and RIPK3, was below detection limits in kidney epithelial, cardiac muscle and resident brain cells, but was frequently detected in progenitor and immune barrier cell populations (**Fig. S2A**; (*41*)).

Close inspection of sites where the necroptotic pathway was constitutively expressed showed unexpected layers of spatial regulation (**Fig. 2A, B**). In the epithelial barrier of the ileum, Caspase-8 expression was lower in crypts and higher at villi tips, whereas RIPK3 levels peaked in the transit amplifying region and decreased towards the villus tip (**Fig. 2Ai**). In the colonic epithelial barrier, both Caspase-8 and RIPK3 exhibited higher expression in the base of the crypt and decreased towards the tip of the crypt (**Fig. 2Aii**). It is noteworthy that expression patterns of Caspase-8 and RIPK3 differ between the small and large intestine because these organs exhibit distinct cell death responses to the same inflammatory stimuli (e.g. TNF) or genetic deficiency (e.g. deletion of *Casp8* or *Fadd*) (*42-45*). In liver, Kupffer cells expressed Caspase-8, RIPK1 and RIPK3 (**Fig. 2Aiii**; arrowheads), whereas hepatocytes expressed Caspase-8 and RIPK1, but not RIPK3. Interestingly, Caspase-8 levels were higher in pericentral hepatocytes than in periportal hepatocytes (**Fig. 2Aiii**; arrow). Zonation of the necroptotic pathway was also evident in the spleen, with Caspase-8, RIPK1, RIPK3 and MLKL levels peaking in the marginal zone where circulating antigens are trapped for immune presentation (**Fig. 2A,B** and **Fig. S2B**). Prior spatial transcriptomics data support the conclusion that necroptotic potential is zoned along the intestinal crypt-to-villus axis (**Fig. S2C**; (*46*)) and along the hepatic central-to-portal axis (**Fig. S2D**; (*47*)). We also performed spatial transcriptomics on mouse spleen to confirm that necroptotic potential peaks in the marginal zone (**Fig. S2E-G**).

The expression of RIPK3 appears to be under particularly strict spatial control. For example, in the ileum, RIPK3 levels were high in fast-cycling epithelial progenitors, but low in adjacent, terminally differentiated Paneth cells (**Fig. 2Ai**; open arrowhead). Published single cell transcriptomics data supports that Paneth cells express low levels of RIPK3 (*48*). As another example, RIPK3 levels were high in fast-cycling colonic epithelial cells, but undetectable in slow-cycling renal epithelial cells (**Fig. 1D**). These observations suggest that RIPK3 expression is linked to cell turnover. Indeed, across 103 cell ontologies in the *Tabula Muris* dataset, gene expression of cell cycle markers *Top2a* and *Mki67* correlated with the expression of *Ripk3,* but not *Ripk1* (**Fig. 2C** and **Fig. S2A**; (*41*)). Prior cell cultures studies further suggest that the expression and function of RIPK3 fluctuates during the mitotic cell cycle (*49, 50*).

Altogether, by applying a set of optimised immunohistochemistry protocols to multiple organs, we have found that necroptotic pathway is preferentially expressed at fast-cycling immune barriers under basal conditions. Such targeted expression is consistent with the evolutionary origin of necroptosis being an anti-pathogen defence measure (*1, 2, 6*). We further find that necroptotic potential is spatially graded along barriers such as the intestinal mucosa. These gradations in the availability of cell death mediators along barriers likely allow multiple cell death programs to be flexibly deployed against invading pathogens (*51, 52*).

Inflammation, dysbiosis or immune challenge trigger local changes in RIPK3 expression

To demonstrate scalability, we used automated immunohistochemistry to characterise the expression of Caspase-8, RIPK1 and RIPK3 across six tissues during TNF-induced Systemic Inflammatory Response Syndrome (SIRS) – a widely-used model of RIPK-dependent pathology (**Fig. 3A;** (*19, 45, 53-55*)). Littermate wild-type mice were intravenously administered TNF, or vehicle, and tissues harvested 9 hours later when symptoms such as hypothermia were manifesting (**Fig. 3B**). No major changes to Caspase-8 or RIPK1 expression were observed after TNF administration, except for an unidentified population of RIPK1-expressing cells appearing at the onset of apoptosis in lymphoid tissues (**Fig3. C-D;** arrowhead). By comparison, RIPK3 was upregulated in intestinal epithelial cells (**Fig. 3E-F**), certain vascular beds (**Fig. 3G-H**) and in liver (**Fig. 3I-J**); the main sites where RIPK1- and RIPK3-signaling during SIRS has been implicated by knockin and knockout mouse studies (*19, 45, 53*). In contrast, RIPK3 levels were not increased in resident cells of the kidney or heart in TNF-treated mice. Our data therefore suggest that targeted upregulation of RIPK3 in resident cells of the gut and liver underlies RIPK-mediated pathology in SIRS. TNF-treatment also changed the pattern of RIPK3 expression in the intestine, potentially skewing cell death responses in the inflamed gut (**Fig. 3E-F**). It was surprising that RIPK3 was detected in peri-portal hepatocytes after TNF administration, given that RIPK3 is epigenetically silenced in hepatocytes under basal conditions (*56*). Collectively, our immunohistochemical characterisation of the SIRS mouse model leads us to propose that the regulation of RIPK3 is akin to an acute phase reactant, with hepatic and intestinal expression that rapidly increases in response to inflammation.

Next, we addressed whether microbiota-depletion affects necroptotic pathway expression. This question was prompted by studies showing that antibiotics offer protection in various models of intestinal necroptosis (*43, 57-59*). As shown in **Fig. 4A**, a litter of wild-type mice was split into two cages and the water for one cage was supplemented with antibiotics for 6 days. As expected, the cecum of antibiotic-treated mice was enlarged and canonical anti-microbial factors such as lysozyme and REG-3β were reduced in the ileum, but not the spleen, of antibiotic-treated mice (**Fig. 4B-C**). These predictable changes to microbiota-depletion also coincided with a lowering of RIPK3 gene and protein expression in the ileum, but not the spleen (**Fig. 4B-C**). MLKL gene expression was also suppressed in the ileum, but not the spleen, of antibiotic-treated mice (**Fig. 4B**). In contrast, Caspase-8 gene and protein expression in the ileum were unaffected by microbiota-depletion, whereas ileal RIPK1 protein levels were increased by antibiotic treatment (**Fig. 4B-C**). Similar trends were observed by immunohistochemistry, with epithelial Caspase-8 expression remaining constant, while RIPK1 levels were elevated and RIPK3 expression reduced in the crypt and transit amplifying regions of the ileum in antibiotic-treated mice (**Fig. 4D**). Unexpectedly, immunohistochemistry also showed that microbiota-depletion triggered cytoplasmic accumulations of RIPK1 and RIPK3 in enterocytes at villi tips (**Fig. 4D**; arrowheads). These clusters of RIPK1 and RIPK3 are reminiscent of chylomicrons (*60, 61*), and were not observed in the colon of antibiotic-treated mice. Overall, we find that expression of the necroptotic pathway locally responds to changes in the microbiome. This response is spatially restricted to the ileum, zoned along the crypt-to-villus axis, and warrants further investigation given that dysbiosis often occurs in cell death-associated disorders such as Crohn's disease (*62*).

Lastly, we used automated immunohistochemistry to uncover a potential non-necroptotic role for RIPK3 in adaptive immunity. We immunised wild-type mice with the model ligand, NP-KLH (4-hydroxy-3-nitrophenylacetyl hapten conjugated to keyhole limpet hemocyanin), and harvested tissues 14 days later when antigen-specific antibody responses are detectable (**Fig. S3A**). No changes in the levels or zonation of Caspase-8, RIPK1 or RIPK3 were noted in the ileum of immunised mice and no marked differences in the expression of Caspase-8, RIPK1 or MLKL were observed in the spleen of immunised mice. However, RIPK3 levels were markedly elevated in Ki67^{+} germinal centres (**Fig. S3B**; arrowheads). This finding suggests that RIPK3 may have a non-necroptotic role in antibody production. To investigate this possibility, *Ripk3*$^{+/+}$, *Ripk3*$^{+/-}$ and *Ripk3*$^{-/-}$ littermate mice were immunised with NP-KLH and humoral immune responses measured in blood and spleen 14 days later (**Fig. S3C-H**). *Ripk3*-deficiency did not alter circulating white blood cell counts (**Fig. S3C**), or the total number of class-switched B cells in the spleen (**Fig. S3D,E**), or the amount of circulating NP-specific antibodies after immunisation (**Fig. S3G,H**). Thus, consistent with prior studies (*63*), RIPK3 does not overtly affect early antigen-specific antibody responses. However, the number of CD138^{+} NP-specific plasma cells was reduced in the spleen of immunised *Ripk3*$^{-/-}$ mice (**Fig. S3F**), suggesting that RIPK3 may have an ancillary role during antigen-driven immunity. Thus, future studies should explore a role of RIPK3 in splenic germinal centres, especially given that RIPK3 has an undefined non-necroptotic role during lymphoproliferative disease (*64*).

In summary, by employing a toolbox of automated immunohistochemical stains, we find that expression of the necroptotic pathway, in particular RIPK3, is responsive to inflammation, dysbiosis or immunisation. These context-specific changes are tightly regulated across space and time, underscoring the need for robust, scalable, *in situ* assays to pinpoint necroptotic pathway expression and activation.

Automated immunohistochemical detection of the human necroptotic pathway

Important differences exist between the human and mouse necroptotic pathways (*29, 30, 65-69*). For instance, the primary sequence of RIPK3 and MLKL are poorly conserved between species (*65*), and humans uniquely express Caspase-10 which likely negates necroptotic signaling (*70, 71*). Thus, in parallel to developing assays for the murine necroptotic pathway, sixteen antibodies against Caspase-8, Caspase-10, RIPK1, RIPK3 or MLKL were tested on wild-type versus knockout formalin-fixed paraffin-embedded HT29 human cells via immunoblot, and then iteratively optimised for immunohistochemistry (see *Methods* and **Fig. S4**). While RIPK3 and Caspase-10 remained refractory to immunohistochemical detection (**Fig. S4**), five automated immunohistochemistry protocols were developed for human Caspase-8, RIPK1, or MLKL (**Fig. S4**). These automated immunohistochemistry protocols can detect the low levels of Caspase-8, RIPK1 and MLKL found in human cells during TNF-induced necroptosis, while simultaneously detecting the pool of Caspase-8, RIPK1 and MLKL held at necrosomes (**Fig. 5**; arrowhead). Indicative of specificity, Caspase-8$^+$ RIPK1$^+$ MLKL$^+$ necrosomes were observed during TNF-induced necroptosis, but not during treatment with TNF alone or during TNF-induced apoptosis (**Fig. 5**). Notably, the translocation of Caspase-8 and RIPK1, but not MLKL, to necrosomes could also be detected in mouse dermal fibroblasts undergoing TNF-induced necroptosis (**Fig. S5**). This species-dependent difference is likely due to dissimilarities in the interaction between RIPK3 and MLKL, which is thought to be more transient in mouse than human cells (*68*). Next, by combining automated immunohistochemistry with high-resolution digital slide scanning (~250nm resolution) and customised image segmentation, we show that necrosomes can be detected and quantified across a large population of cells in an unbiased manner (**Fig. 5B-C**). We observed that the accuracy of segmenting human Caspase-8 or MLKL at necrosomes is higher than that of RIPK1, because the small puncta formed by necrosomal RIPK1 are near the resolution limit of existing brightfield slide scanners (**Fig. 5C**). Nonetheless, as necrosomes are a pathognomonic feature of necroptotic signaling, we propose that machine-based detection of necrosomes could be developed into a diagnostic assay for pinpointing necroptosis in formalin-fixed human patient biopsies.

Necrosome immunodetection in patients with IBD

Ulcerative colitis (UC) and Crohn's disease (CD) are the main types of inflammatory bowel disease (IBD) (*72, 73*). The causes of adult onset IBD are multifactorial (*74, 75*). While many studies show that excess necroptosis promotes IBD-like pathology in mice (*18, 42, 58, 76-79*), few studies have examined the prevalence of necroptosis in IBD patients (*80-82*). One completed Phase II trial of a RIPK1 inhibitor in UC failed to demonstrate clinical efficacy (*83*). Another 7 clinical and preclinical trials of RIPK1 inhibitors in IBD are underway. Thus, the role of necroptosis in IBD requires further investigation. We collected intestinal biopsies from adults with UC, CD and non-IBD patients (**Fig. 6A**). To capture the chronology of disease, biopsies were collected from endoscopically ‘non-inflamed’, ‘marginally inflamed’ and ‘inflamed’ intestinal tissue from each IBD patient. The grading of inflammation was verified by blinded histopathology scores (**Fig. 6B**). Cell death signaling in biopsies from each location and endoscopic grade was assessed by immunoblot (**Fig. 6C** and **Table S1**). To assist interpretation, patient samples (**Fig. 6C**; blue annotations) were immunoblotted alongside lysates from HT29 cells undergoing apoptosis or necroptosis (**Fig. 6C**; red annotations). Apoptotic signaling was inferred from increases in the conversion of pro-Caspase-3, -8 and -10 into their active cleaved forms (**Fig. 6C**; open arrowheads). Necroptotic signaling was inferred from increases in the abundance of phosphorylated RIPK3 and MLKL, relative to their non-phosphorylated forms (**Fig. 6C**; asterisks). This approach showed that cell death signaling is elevated in intestinal tissue from IBD patients relative to non-IBD patients, especially in inflamed intestinal biopsies from IBD patients (**Fig. 6C**). However, marked heterogeneity in the prevailing form of cell death was apparent in both UC and CD patients; with apoptosis dominant in some IBD cases (**Fig. 6C**; patients B and F), and necroptosis dominant in others (**Fig. 6C**; patients D and H). Given the ongoing development of RIPK1 inhibitors, it is noteworthy that phosphorylated MLKL coincided with phosphorylated RIPK1 in some, but all not IBD patients (**Fig. 6C**; patients D and H). The reason why cell death mechanisms vary between patients is currently unknown. Collectively, we find that cell death signaling increases in the inflamed gut, supporting the idea that cell death inhibitors are a potential treatment option for IBD. Whether apoptosis or necroptosis manifests in an individual IBD patient appears to be highly variable, highlighting the need for diagnostic approaches, such as automated immunohistochemistry, to identify patients that may benefit from anti-necroptotic therapy.

Having identified necroptotic signaling in IBD ‘patient D’ relative to non-IBD ‘patient C’, we applied our automated immunohistochemistry panel to biopsies collected from these same patients, taken at the same time and from the same intestinal locations (**Table S1**). No obvious changes to epithelial RIPK1 and MLKL were evident between patients C and D. By comparison, cytoplasmic clusters of Caspase-8 were evident in the epithelial layer of the inflamed biopsy from patient D (**Fig. 6D**; arrowheads). As these cytoplasmic clusters of Caspase-8 were reminiscent of the Caspase-8$^+$ necrosomes in necroptotic HT29 cells (**Fig. 5**), we used the same high-resolution digital slide scanning and unbiased image segmentation approach as before. This quantitation showed that the number of intraepithelial Caspase-8$^+$ clusters was low in non-IBD patient C and increased with inflammation in IBD patient D (**Fig. 6E**). This trend mirrors the levels of necroptotic signaling in IBD patient D (**Fig. 6B**), suggesting that cytoplasmic clusters of Caspase-8$^+$ may represent bona fide necrosomes. This case study provides proof-of-principle that automated immunohistochemical detection of necrosomes is feasible and could be developed into a diagnostic assay for pinpointing necroptosis in clinical practice.

Discussion

The difficulty of reliably detecting necroptotic signaling in fixed tissues has been a longstanding issue, generating confusion and conflicting results in the literature. To address this problem, we optimised the immunohistochemical detection of Caspase-8, RIPK1, RIPK3 and MLKL in formalin-fixed paraffin-embedded samples. While our prior studies immunostained non-crosslinking fixed monolayers (*33, 38*), here we used formalin-fixed paraffin-embedded specimens consistent with standard practice in hospital pathology and research departments around the world. In total, over 280 different immunostaining conditions were tested, yielding 12 automated immunohistochemistry protocols that we anticipate will be of broad utility to the cell death community and drive new insight into the causes, circumstances, and consequences of necroptosis. To assess the reliability of our automated protocols, we benchmarked our immunostaining results against data obtained using other methodologies. For instance, our automated immunohistochemistry protocols produced results that were comparable to public resources generated using proteomic, single cell transcriptomic, and spatial transcriptomic approaches (*41, 46, 47, 84*). Confidence was also taken from the similar staining patterns produced between three Caspase-8 antibodies (clones D53G2, 3B10 and 1G12), between two RIPK3 antibodies (clones 8G7 and 1H12), and between mouse and human intestinal tissue using the same

RIPK1 antibody (clone D94C12). Thus, multiple lines of evidence suggest that the automated protocols described herein are specific and sensitive.

Our approach for optimising and interpreting immunohistochemical signals relied upon quantitative analyses that carries important technical considerations. First and foremost, the signals produced by immunohistochemistry are non-linear (*85*). Moreover, before quantitation, we digitally unmixed immunosignals from the haematoxylin counterstain, which is another non-linear transformation of signal intensity (*86*). Thus, only relative changes in expression levels were inferred from changes in immunohistochemical signal intensity. Because of this caveat, we only compared and quantified immunosignals between closely matched specimens, such as corresponding wild-type and knockout samples where both samples were sectioned at the same time, mounted on the same slide, and stained and imaged contemporaneously. To aid quantitation, all our immunohistochemistry protocols were developed to produce unsaturated signals. One final salient point is that this study used automated embedding and immunostaining procedures, with all quantification using macros that analyse a high number (typically thousands) of cells per sample. Thus, the automated immunohistochemistry protocols described herein can be used for quantitative purposes, but only when comparing closely matched specimens, and ideally with supporting data from alternative methodologies such as spatial transcriptomics. These recommendations reduce, but do not eliminate, the need to use knockout samples as a control for specificity.

The phosphorylated forms of RIPK1, RIPK3 and MLKL are the most widely used markers of necroptotic signaling (*65*). Accordingly, prior attempts to detect necroptotic signaling in fixed specimens have focussed on phospho-RIPK1, -RIPK3 and -MLKL (*7, 16, 21, 33, 35, 38-40, 87-89*). However, there are drawbacks with this approach: 1) antibodies against phosphorylated epitopes in RIPK1/3 and MLKL exhibit much poorer signal-to-noise properties than do antibodies against unphosphorylated epitopes in RIPK1/3 and MLKL

(*38*); 2) while knockout samples are sufficient for verifying non-phospho-signals, multiple controls are needed to authenticate phospho-signals (e.g. resting, knockout and phosphatase pre-treated samples; and 3) because only a small fraction of RIPK1/3 and MLKL is phosphorylated during necroptosis these phospho-species are inherently more difficult to detect than their unphosphorylated counterparts. Indeed, as is standard practice when detecting necroptosis via immunoblot, the immunohistochemical detection of phospho-RIPK1, -RIPK3 and -MLKL can only be interpretated when their unphosphorylated forms are also detected. For these reasons, we focused on the immunohistochemical detection of unphosphorylated RIPK1, RIPK3 and MLKL, and used the immunodetection of necrosomes as a marker of necroptotic signaling.

It was surprising that expression of the necroptotic pathway was heavily restricted under steady-state conditions in mice. That fast-cycling progenitors and immune barrier cells are the dominant expressors of RIPK3 and/or MLKL suggests that the existential role of necroptosis is to protect the host from invading pathogens. The phenotypes and cell types affected in mice carrying activation-prone polymorphisms in *Mlkl* also supports the view that the ancestral role of necroptosis lies in innate immunity (*90-92*). The absence of necroptotic pathway expression in slow-cycling cell populations was equally striking, with RIPK3 and/or MLKL undetectable in resident cells of the heart (except for certain fibroblasts), the brain (except for leptomeningeal vessels), the kidney and the liver (except for Kupffer cells) in mice under basal conditions. These observations challenge a vast body of literature, which we believe highlights the need for robust well-controlled methodologies. These results lead us to propose that slow-cycling cell populations ensure longevity by avoiding inadvertent necroptosis. The observation that RIPK3 expression is rapidly derepressed in hepatocytes during inflammation supports the notion that long-lived cells actively suppress necroptotic signaling, but only in the absence of challenge. The derepression of RIPK3 may reconcile the contribution of necroptosis in inflammatory disorders such as hepatocellular carcinoma (*93*), acute myocardial infarction (*13*), acute ischemic stroke (*94*) and kidney ischemia-reperfusion injury (*15*). Notably, the Human Protein Atlas lacks immunohistochemical data for RIPK3 and MLKL, and therefore it remains unknown whether the necroptotic pathway is similarly restricted in humans (*95*).

To exemplify the utility of our approach, we applied our full immunohistochemistry panel to determine whether inflammation, dysbiosis or immunisation alter necroptotic pathway expression. Each of these challenges altered necroptotic pathway expression in a manner that chiefly involved local shifts in RIPK3 expression. This profiling of the necroptotic pathway yielded many unexpected observations, including: 1) RIPK3 expression is disinhibited in hepatocytes after TNF administration; 2) RIPK3 expression is suppressed in the gut during antibiotic administration with RIPK1/3 coalescing into unidentified cytoplasmic clusters in epithelial cells at the villus tip; and 3) RIPK3 expression is uniquely upregulated in splenic germinal centres after immunisation. While the mechanistic basis for these findings warrants future attention, their initial description here illustrates the benefits of studying the necroptotic pathway using automated immunohistochemistry.

We provide proof-of-principle that the immunodetection of necrosomes can be used as an *in situ* marker of necroptotic signaling in IBD patients. To reach this conclusion, we developed a suite of automated immunohistochemical protocols to detect the relocation of necroptotic effectors into necrosomes and validated the presence of necroptotic signaling in closely matched biopsies from IBD patients using immunoblot. Collectively, these experiments show that Caspase-8$^+$ RIPK1$^+$ MLKL$^+$ necrosomes can be readily detectable under idealised cell culture conditions, that elevated necroptotic signaling occurs in a subset of IBD patients, and that cytoplasmic clustering of Caspase-8 correlated with necroptotic signaling across a set of biopsies. Why clusters of Caspase-8, but not clusters of RIPK1 or MLKL, were detectable in biopsies with active necroptotic signaling is unknown, but may be due to technical limitations (e.g. resolution limit) or gaps in our understanding of how necroptosis manifests *in vivo*. Another important issue is whether the immunohistochemical detection of Caspase-8$^+$ clusters can be used to quantify necroptotic signaling in larger cohorts of IBD patients and in patients with other clinical indications. Notwithstanding these issues, the detection of *in situ* changes in necroptotic pathway expression in a scalable, quantitative, and automated manner represents a major leap forward in the capacity to pinpoint when and where necroptosis arises in health and disease.

Materials and methods

Materials

Primary antibodies were rat anti-mouse Caspase-8 (clone 3B10; RRID:AB_2490519; 1g/L produced in-house (*96*) and available from AdipoGen Cat#AG-20T-0138), rat anti-mouse Caspase-8 (clone 1G12; RRID:AB_2490518; 1g/L produced in-house (*96*) and available from AdipoGen Cat#AG-20T-0137), rabbit anti-Caspase-8 (clone D35G2; RRID:AB_10545768; Cell Signaling Technology Cat#4790), rabbit anti-phospho-RIPK1 (clone D813A; RRID:AB_2799268; Cell Signaling Technology Cat#44590S), mouse anti-RIPK1 (clone 38/RIP; RRID:AB_397831; 0.25g/L BD Biosciences Cat#610459), mouse anti-RIPK1 (clone 334640; RRID:AB_2253447; 0.5g/L; R&D Systems Cat#MAB3585), rabbit anti-RIPK1 (clone D94C12; RRID:AB_2305314; Cell Signaling Technology Cat#3493), rabbit anti-RIPK3 (clone 18H1L23; RRID: AB_2866471; 0.5g/L; Thermo Fisher Scientific Cat#703750), rabbit anti-phospho-RIPK3 (clone D6W2T; RRID:AB_2800206; Cell Signaling Technology Cat#93654), rat anti-RIPK3 (clone 1H12; 2g/L produced in-house (*38*)), rat anti-RIPK3 (clone 8G7; RRID: RRID:AB_2940810; 2g/L produced in-house (*6*) and available from Millipore Cat#MABC1595), rabbit anti-phospho-MLKL (clone EPR9514; RRID:AB_2619685; Abcam Cat#ab187091; (*35*)), mouse anti-MLKL (clone

3D4C6; RRID:AB_2882029; 1.957g/L; Proteintech Cat#66675-1-IG), rabbit anti-mouse MLKL (clone D6W1K; RRID:AB_2799118; Cell Signaling Technology Cat#37705), rat anti-mouse MLKL (clone 5A6; RRID:AB_2940800; 50g/L produced in-house (*38*) and available from Millipore Cat#MABC1634), rat anti-MLKL (clone 3H1; RRID:AB_2820284; 2g/L produced in-house (*32*) and available from Millipore Cat# MABC604), mouse anti-Caspase-10 (clone 4C1; RRID:AB_590721; 1g/L; MBL International Cat# M059-3), mouse anti-Caspase-8 (clone B.925.8; RRID:AB_10978471; 0.619g/L Thermo Fisher Scientific Cat# MA5-15226), mouse anti-Caspase-8 (clone 5D3; RRID:AB_590761; 1g/L; MBL International Cat#M058-3), rat anti-human RIPK3 (clone 1H2; RRID:AB_2940816; 2g/L produced in-house (*6*) and available from Millipore Cat# MABC1640), rabbit anti-human RIPK3 (clone E1Z1D; RRID:AB_2687467; Cell Signaling Technology Cat# 13526), rat anti-human MLKL (clone 7G2; RRID:AB_2940818; 2g/L Millipore Cat# MABC1636), rat anti-human MLKL (clone 10C2; RRID:AB_2940821; 2g/L Millipore Cat# MABC1635), rabbit anti-MLKL (clone 2B9; RRID:AB_2717284; 1g/L; Thermo Fisher Scientific Cat#MA5-24846), rabbit anti-MLKL (clone EPR17514; RRID:AB_2755030; 1.9g/L; Abcam Cat# ab184718), mouse anti-GAPDH (clone 6C5; RRID:AB_2107445; 1g/L; Millipore Cat# MAB374), rabbit anti-smooth muscle actin (clone D4K9N; RRID:AB_2734735; Cell Signaling Technology Cat#9245S), rabbit anti-lysozyme (clone EPR2994(2); RRID:AB_10861277; Abcam Cat#108508), cleaved-caspase 3 (Cell Signaling Technology, #9661), Ki67 (Cell Signaling Technology, #12202). The concentration of antibodies from Cell Signaling Technology is often not provided and thus was not listed here.

Secondary antibodies for immunoblotting were horseradish peroxidase (HRP)-conjugated goat anti-rat immunoglobulin (Ig) (Southern BioTech Cat#3010-05), HRP-conjugated goat anti-rabbit Ig (Southern BioTech Cat#4010-05) and HRP-conjugated goat anti-mouse Ig (Southern BioTech Cat#1010-05).

Reagents for immunohistochemistry were HRP-conjugated anti-rabbit Ig (Agilent Cat# K400311-2), HRP-conjugated anti-mouse Ig (Agilent Cat# K400111-2), MACH4 universal HRP-Polymer (Biocare Medical Cat#M4U534L), ImmPRESS HRP-conjugated anti-rat IgG for human samples (Vector Laboratories CatcVEMP740450), HRP-conjugated anti rat IgG for mouse samples (R&D Systems Cat#VC005-125), Rabbit Linker (Agilent Cat#GV80911-2). Epitope Retrieval Solution 1 (Leica Cat#AR9961), Epitope Retrieval Solution 2 (Leica Cat#AR9640), Retrieval Solution Low pH (Agilent Cat#GV80511-2), Retrieval Solution High pH (Agilent Cat#GV80411-2), 3,3'-diaminobenzidine (DAB) substrate (Agilent Cat#GV82511-2 or GV92511-2), Dako REAL Peroxidase-blocking reagent (Agilent S202386-2), bluing reagent (Leica, 3802915), Background Sniper (Biocare Medical Cat#BS966L), Dako Protein Block (Agilent Cat#X0909), 'Normal' block (Agilent Cat#S202386-2), EnVision FLEX TRS High pH (Agilent Cat# GV80411-2), EnVision FLEX TRS Low pH (Agilent Cat# GV80511-2), MACH4 universal HRP polymer (Biocare Medical Cat#M4U534L), and DPX (Trajan Cat#EUKITT).

Mice, research ethics and housing

All experiments were approved by The Walter and Eliza Hall Institute (WEHI) Animal Ethics Committee, Australia, in accordance with the Prevention of Cruelty to Animals Act (1986), with the Australian National Health and Medical Research Council Code of Practice for the Care and Use of Animals for Scientific Purposes (1997), and with the ARRIVE guidelines (*97*). Mice were housed at the WEHI animal facility under specific pathogen-free, temperature- and humidity-controlled conditions and subjected to a 12 h light/dark cycle with ad libitum feeding. Mice without functional MLKL alleles (*Mlkl*$^{-/-}$) have been described previously (*32*). Mice without functional RIPK3 alleles (*Ripk3*$^{-/-}$) have been described previously (*98*). Mice without functional alleles of RIPK1, RIPK3 and Caspase-8

(*Ripk1*$^{-/-}$ *Ripk3*$^{-/-}$*Casp8*$^{-/-}$ triple knockout mice) and *Ripk3*$^{-/-}$*Casp8*$^{-/-}$ double knockout mice have been described previously (*99*) and were derived from reported mouse strains (*63, 100, 101*).

Mouse tissue lysate preparation

Mouse tissues were homogenised with a stainless steel ball bearing in a Qiagen TissueLyzer II (30 Hz, 1min) in ice-cold RIPA buffer (10mM Tris-HCl pH 8.0, 1mM EGTA, 2mM MgCl2, 0.5% v/v Triton X100, 0.1% w/v sodium deoxycholate, 0.5% w/v sodium dodecyl sulfate (SDS) and 90mM NaCl) supplemented with 1x Protease & Phosphatase Inhibitor Cocktail (Cell Signaling Technology Cat#5872) and 100 U/mL Benzonase (Sigma-Aldrich Cat#E1014). 1mL of RIPA buffer per 25mg of tissue was used for homogenisation.

Immunoblot

For **Fig. S1** and **Fig. S4**, RIPA lysates were boiled for 10min in Laemmli sample buffer (126□mM Tris-HCl, pH 8, 20% v/v glycerol, 4% w/v sodium dodecyl sulfate, 0.02% w/v bromophenol blue, 5% v/v 2-mercaptoethanol) and fractionated by 4-15% Tris-Glycine gel (Bio-Rad Cat#5678084) using Tris-Glycine running buffer (0.2M Tris-HCl, 8% w/v SDS, 0.15M glycine). After transfer onto nitrocellulose, membranes were blocked in 1% w/v bovine serum albumin (BSA) or 5% w/v skim cow's milk in TBS+T (50mM Tris-HCl pH7.4, 0.15M NaCl, 0.1 v/v Tween20), probed with primary antibodies (1:2000 dilution for rat primary antibodies or 1:1000 for other primary antibodies; supplemented with 0.01% w/v sodium azide; see Materials above) overnight at 4^{o}C, washed twice in TBS+T, probed with an appropriate HRP-conjugated secondary antibody (see Materials above), washed four times in TBS+T and signals revealed by enhanced chemiluminescence (Merck Cat#WBLUF0100) on a ChemiDoc Touch Imaging System (Bio-Rad). Between probing with primary antibodies from the same species, membranes were incubated in stripping buffer (200 mM glycine pH 2.9, 1% w/v SDS, 0.5 mM TCEP) for 30 min at room temperature then re-blocked.

For **Fig. 4** and **Fig. 6**, RIPA lysates were boiled for 10min in Laemmli sample buffer (126 mM Tris-HCl, pH 8, 20% v/v glycerol, 4% w/v SDS, 0.02% w/v bromophenol blue, 5% v/v 2-mercaptoethanol) and fractionated by 4–12% Bis-Tris gel (Thermo Fisher Scientific Cat#NP0335BOX) using MES running buffer (Thermo Fisher Scientific Cat#NP000202). After transfer onto polyvinylidene difluoride (Merck Cat# IPVH00010), gels were Coomassie-stained as per manufacturer's instructions (Thermo Fisher Scientific Cat#LC6060) and membranes were blocked in 5% w/v skim cow's milk in TBS+T and then probed as above.

Mouse tissue fixation

Tissues were immediately harvested after euthanasia and placed in 10% v/v Neutral Buffered Formalin (NBF) (Confix Green; Australian Biostain Cat#AGFG.5L). A ratio of one part tissue to >10 parts formalin was used. Unless stipulated, tissues were incubated in formalin at room temperature for 24-72 hours.

Paraffin embedding, microtomy and immunostaining

Unless stipulated, formalin-fixed cells/tissues were paraffin embedded using the standard 8 hour auto-processing protocol of the Tissue-Tek VIP® 6 AI Tissue Processor (Sakura Finetek USA). Paraffin embedded cells/tissues were cut in 4µm-thick sections onto adhesive slides (Menzel Gläser Superfrost PLUS). Haematoxylin and eosin staining was done on the Autostainer XL (Leica ST5010). Immunohistomechistry was performed on an automated system: the Bond RX (Leica) or the DAKO OMNIS (Agilent). While all automated immunohistochemistry protocols will be fully stipulated in Supplementary File x upon final publication, a brief overview of these methods is as follows: Step 1 was deparaffinisation (Phase 1: Clearify Clearing Agent; Phase 2: deonised water), Step 2 was heat-induced antigen retrieval (EnVision FLEX TRS, High pH or Low pH retrieval buffer. Treatment time was antibody-dependent), Step 3 was endogenous peroxidase blocking (Dako REAL Peroxidase-blocking reagent. Incubation time was antibody-dependent), Step 4 was protein blocking (Background Sniper, Dako Protein Block or Normal block. Incubation 10 minutes), Step 5 was primary antibody incubation (dilutions and incubation times were antibody-dependent), Step 6 was option signal amplification (amplification technique was antibody-dependent. Rabbit linker. Incubation 15 minutes), Step 7 was secondary reagent with horseradish peroxidase (anti-rabbit HRP polymer, anti-mouse HRP polymer, MACH4 universal HRP polymer, ImmPRESS anti-rat HRP polymer, anti-rat HRP polymer and in-house HRP signal amplification detection. Reagent and incubation was antibody-dependent), Step 9 was signal detection (chromogen-substrate DAB. Onboard mixing and incubation 10 minutes), Step 10 was counterstaining (in-house made Mayer’s Haematoxylin for 1 minute followed by Bluing reagent for 1 minute), Step 11 was dehydration, mounting in DPX and coverslipping using Leica CV5030 platform.

Image acquisition

Unless stipulated, slides were scanned on: 1) 3D Histech Pannoramic Scan II (objective: magnification 20x, numerical aperture 0.8, media dry; software: Pannoramic SCAN 150 1.23 SP1 RTM and SlideViewer 2.8.178749), or 2) Olympus VS200 (objective: 20x, numerical aperture 0.8, media dry; software: Olympus VS200 ASW 3.41). Where higher resolution was required, slides were scanned on the Olympus VS200 using the 60x objective (numerical aperture 1.42, media oil).

Post-acquisition processing of displayed micrographs

All displayed micrographs were acquired with VS200 Research Slide Scanner (Olympus). Representative full-resolution 8-bit RGB micrographs of the WT and KO tissues/cells were imported into ImageJ 1.53t (*102*). Brightness-and-contrast was adjusted to 0-235 units and then gamma levels adjusted by 1-1.5-fold. Capture settings and post-acquisition image transformations were held constant between any micrographs that were being compared.

Immunohistochemistry signal-to-noise ratio (S/N) analysis

Sections of wild-type (WT) and corresponding knockout (KO) tissues/cells on the same slide were immunostained and imaged. Representative full-resolution 8-bit RGB micrographs of the WT and KO tissues/cells were imported into ImageJ 1.53t (*102*) and the ‘H-DAB’ function of the ‘Colour Deconvolution 2’ plugin (*86*) was used to unmix the DAB and hematoxylin channels. A dilated mask of the auto-thresholded hematoxylin channel was applied to the corresponding DAB channel to select an area-of-interest, and then a histogram of pixel intensities from the DAB channel for both the WT and KO micrographs was determined. The ‘WT histogram’ was then divided by the ‘KO histogram’ to yield a S/N curve (see Fig1A for example). A weighted integral of the S/N curve was calculated as a numerical index of specificity (red box in Fig1A). The representative micrographs used to calculate S/N curves were of equivalent size, included >1000 cells per sample and their gamma levels unchanged.

Quantitation of zonation via immunohistochemistry

Representative full-resolution 8-bit RGB micrographs of the WT tissues were imported into ImageJ 1.53t (*102*). Brightness-and-contrast was adjusted to 0-235 units and the ‘H-DAB’ function of the ‘Colour Deconvolution 2’ plugin (*86*) was used to unmix the DAB and hematoxylin channels. The look-up-table for the DAB channel was converted to grayscale and pixel values inverted. The ‘Segmented Line tool’ was used to draw a line (27.4µm wide to approximate 2 cell widths) along the main axis of the following zones: 1) crypt base to villi tip in the ileum, 2) crypt base to crypt tip in the colon, 3) peri-central hepatocytes to peri-portal hepatocytes, and 4) white matter to red pulp in the spleen. The ‘Plot Profile tool’ was used to quantify the immunosignal along the drawn axis, which was then averaged across N=10-20 representative zones per mouse.

Quantitation of endothelial RIPK3 levels via immunohistochemistry

Sections were subjected to automated immunohistochemistry for smooth muscle actin (SMA) and RIPK3 (see Supplementary File x). SMA signals were detected with a brown DAB product. RIPK3 signals were detected with a pink DAB product. Sections were not counterstained with hematoxylin. Full-resolution 8-bit RGB micrographs (taken with 60x objective; Olympus VS200) were imported into Image J 1.53t (*102*) and endothelial RIPK3 levels analysed using a custom semi-automated macro in a non-blinded manner. In brief, cross-sections of individual SMA$^+$ vessels were chosen, SMA and RIPK3 signals were unmixed using the ‘Colour Deconvolution 2’ plugin (*86*). An auto-thresholded mask of the SMA$^+$ intima was then used to segment the endothelial area. The total RIPK3 signal in this endothelial area was expressed per unit area. This procedure was repeated for N=50 vessels per mouse.

Quantitation of hepatocyte RIPK3 levels via immunohistochemistry

Sections were subjected to automated immunohistochemistry for RIPK3 (see Supplementary File x). RIPK3 signals were detected with brown DAB product and sections were counterstained with hematoxylin. Representative full-resolution 8-bit RGB micrographs (taken with the 60x objective; Olympus VS200) were imported into Image J

1.53t (*102*) and RIPK3 levels within individual hepatocytes analysed using a custom fully-automated macro. In brief, haematoxylin-stained nuclei were unmixed from the RIPK3 signal using the 'Colour Deconvolution 2' plugin (*86*). Nuclei were segmented using the 'Analyze Particles' function of Image J and hepatocyte nuclei distinguished from Kupffer cell nuclei on the basis of their larger size and circularity. The total RIPK3 signal in the cytosolic area surrounding hepatocyte nuclei was segmented, measured and expressed per unit area. N=90 hepatocytes per mouse were measured.

Quantitation of Kupffer cell RIPK3 levels via immunohistochemistry

Sections were subjected to automated immunohistochemistry for RIPK3 (see Supplementary File x). RIPK3 signals were detected with brown DAB product and sections counterstained with hematoxylin. Representative full-resolution 8-bit RGB micrographs (taken with the 60x objective; Olympus VS200) were imported into Image J 1.53t (*102*) and RIPK3 levels within individual Kupffer cells were analysed using a custom fully-automated macro. In brief, the RIPK3 signal was unmixed from Hematoxylin using the 'Colour Deconvolution 2' plugin (*86*). An auto-thresholded mask of cells with relatively high expression of RIPK3 was created. This mask, together with the comparatively small and non-circular shape of Kupffer cells, was used to segment individual Kupffer cells. The total RIPK3 signal within each Kupffer cell was then measured and expressed per unit area. N=90 Kupffer cells per mouse were measured.

Quantitation of apoptosis in splenic white pulp via immunohistochemistry

Sections were subjected to automated immunohistochemistry for cleaved Caspase-3 (see Supplementary File x). Cleaved Caspase-3 signals were detected with a brown DAB product and sections counterstained with hematoxylin. Representative full-resolution 8-bit RGB micrographs (taken with the 60x objective; Olympus VS200) were imported into

Image J 1.53t (*102*) and percent area with cleaved Caspase-3 signal was analysed using a custom fully-automated macro. In brief, the cleaved Caspase-3 signal was unmixed from Hematoxylin using the 'Colour Deconvolution 2' plugin (*86*). A predefined threshold (50-255 units) was applied, and its area expressed as a percentage of the total white pulp area. N=20 white pulp lobules per mouse were measured.

Systemic Inflammatory Response Syndrome (SIRS)

Co-housed 8-week-old female C57BL/6J wildtype mice were administered either 300 µg/kg TNF (R&D Systems Cat#410-MT/CF Lot CS152103) in endotoxin-free DPBS or endotoxin-free DPBS alone (Merck Cat# TMS-012-A) via bolus tail vein injection. Core body temperature was measured hourly with a rectal probe. Mice were euthanised via carbon dioxide inhalation 9 hours after injection.

***Tabula muris* analysis**

Robject files of the FACS-based T*abula Muris* (*41*) dataset were downloaded from Figshare. Expression values were normalised and analysed using Seurat v4.3.0 (*103-106*). Within each cell ontology and tissue origin, the percentage of cells with expression values >0 for *Mlkl, Ripk3, Ripk1, Casp8, Mki67 and Top2a* was tabulated and colorised using Excel v16.74 (Microsoft).

Spatial transcriptomics of mouse spleen

To boost germinal centre numbers and size, one adult C57BL/6J mouse was infected intravenously with 1×10^5 *Plasmodium berghei* parasitised red blood cells, and then drug-cured at the onset of disease symptoms as described in (*107*). Twelve days later the mouse was euthanised, spleen dissected, fixed in 10% v/v Neutral Buffered Formalin and paraffin embedded (as above). Sections of formalin-fixed paraffin-embedded spleen were cut onto slides, then spatial enhanced resolution omics-sequencing (stereo-seq) data was generated using pre-release chemistry and MGI sequencers as in (*108*) by BGI, China. The spot-to-spot distance is 500nm and the data is binned to 50x50 spots (25µm^2). Binning was performed in stereopy (https://github.com/BGIResearch/stereopy) before being converted to an anndata file (https://github.com/scverse/anndata). The stereo-seq data was first loaded and pre-processed using the standard Scanpy workflow (https://github.com/scverse/scanpy) and then principal component analysis and Leiden clustering was performed at the bin (50x50) level. Leiden clusters were then plotted using Uniform Manifold Approximation and Projection (UMAP) and on spatial coordinates using the Squidpy package (https://github.com/scverse/squidpy). Scanpy's 'rank_genes_groups' method (https://scanpy-tutorials.readthedocs.io) was used to generate a matrix of gene by cluster populated by corresponding log-fold changes from 1 versus all t-tests. For each zone/cell type of interest a matrix is constructed by subsetting the full gene by cluster matrix generated from 'rank_genes_groups' to just the specific genes of interest. These matrices were reduced to a single column sum aggregated vector. From the vectors of scores for each 'zone' of the spleen (White Pulp, Red Pulp, Germinal Centres, and Marginal Zones), the top 5 scores within the 50th or 75th (depending on expected transcriptional variance within zone) percentile of the maximum are selected and the corresponding Leiden clusters are aggregated hierarchically. After this aggregation of clusters, the 'rank_genes_groups' method is rerun to calculate a new set of gene rankings and log-fold changes for zones rather than clusters. The aggregated scores for genes of interest in each group are calculated for each zone. These scores are the log-fold changes for each gene within each zone. Scores for the *Casp8*, *Ripk1*, *Ripk3*, and *Mlkl* genes are then extracted from the matrices for each 'zone' of the spleen, and each individual cluster for side-by-side comparison in heatmaps. Software version used were Anndata (v0.7.5), Stereopy (v0.12.0), Scanpy (v1.9.2), Squidpy (v1.2.2), Numpy (v1.21.6), Pandas (v1.5.3), Matplotlib (v3.5.2), and Seaborn (v0.12).

Antibiotics administration

Co-housed littermates were split across two cages. The drinking water for one cage was supplemented with 1g/L ampicillin, 1g/L neomycin, 1g/L metronidazole, 0.5g/L enrofloxacin, 2.5g/L meropenem as in (*43*). Antibiotic-supplemented water was replaced after 3 days. To minimise weight loss, both cages were given ad libitum access to Di-Vetelact supplement (Lillelund Pty Ltd). Mice were euthanised after 6 days of treatment.

RNA extraction, library preparation and sequencing

Immediately following dissection, a ~2mm^3 piece of tissue was placed in 0.5mL RNA*later* (Thermo Fisher Scientific Cat#4427575) then stored at -80^{o}C. Samples were thawed, RNA*later* was removed then tissues were transferred into screw-capped tube pre-filled with 350 µl of RA1 buffer of NucleoSPin RNAXS kit (Macherey-Nagel Cat# **SKU:** 740902.250). Tissues were homogenised with 10 pcs of 3 mm Acid- Washed Zirconium Beads (OPS diagnostics Cat# BAWZ 3000-300-23) in a Qiagen TissueLyzer II (30 Hz, 5 minutes). Homogenised samples were centrifuged (1 minute, 11,000 *g*) to remove tissue debris then RNA was purified using Nucleospin RNAXS column kit as per manufacturer's instructions without adding a carrier RNA. The purified RNA was quantified using Qubit™ RNA HS Assay kit (Thermo Fisher Scientific Cat#Q32852) and RNA integrity was visualised in high sensitivity RNA ScreenTape (Agilent Cat# 5067- 5579) using TapeStation 4200 (Agilent Cat# G2991BA). Ten nanograms of RNA were used for preparing indexed libraries using SMARTer Stranded Total RNA-Seq Pico-Input Mammalian kit v.3 (Takara Bio. Cat# SKU: 634487) as per manufacturer's instructions (except that fragementation was performed for 3 minutes of fragmentation at 94 °C and 13 cycles was used for PCR2). The library concentration was quantified by Qubit™ dsDNA Assay kit (Thermo Fisher Cat#Q32851) and library size was determined using D1000 ScreenTape (Agilent Cat# 5067-5582) and visualised in TapeStation 4200. Equimolar amounts of the libraries were pooled and diluted to 750pM for 150-bp paired-end sequencing on a NextSeq2000 instrument (Illumina) using the P2 300- cycle kit v3 chemistry (Illumina Cat# 20046813) as per manufacturer's instructions. To produce the sequences, the base calling and quality scoring was performed by the Real Time Analysis (v2.4.6) software. The FASTQ file generation and de-multiplexing for the samples was performed by the bcl2fastq conversion software (v2.15.0.4).

Murine bulk RNA sequence analysis

The single-end 75□bp were demultiplexed using CASAVAv1.8.2 and Cutadapt (v1.9) was used for read trimming (*109*). The trimmed reads were subsequently mapped to the mouse genome (mm10) using HISAT2 (*110*). FeatureCounts from the Rsubread package (version 1.34.7) was used for read counting after which genes <2 counts per million reads (CPM) in at least 3 samples were excluded from downstream analysis (*111, 112*). Count data were normalised using the trimmed mean of M-values (TMM) method and differential gene expression analysis was performed using the limma-voom pipeline (limma version 3.40.6) (*111, 113, 114*). Adjustment for multiple testing was performed per comparison using the false discovery rate (FDR) method (*115*). Heatmaps of logCPM were generated using pheatmap.

NP-KLH immunization and analysis

Immunisation was performed as previously described (*116*). 8–10-week-old female C57BL/6J wild-type mice received a single intraperitoneal injection of 100□µg 4-hydroxy-

3-nitrophenylacetyl hapten coupled to keyhole limpet hemocyanin (NP-KLH; produced in-house) at a ratio of 21:1 with alum. Fourteen days after immunisation mice were euthanised via CO_2 inhalation and spleens harvested. To determine immune response to NP immunization, single-cell splenic suspensions were stained as described using antibodies to the following surface molecules: CD38 (clone:NIMR-5, in-house), CD19 (clone:1D3, cat #BD552854), IgM (clone:331.12, in-house), IgD (clone:11–26 C, in-house), Gr-1 (clone:RB6-8C5, in-house), CD138 (clone:281.2, cat #BD564068) and IgG1 (clone:X56, cat #BD550874). NP-binding was detected as described (*117*)

Hematological analysis

Blood was collected into a retroorbital capillary and transferred to an EDTA-coated tube. Blood was diluted 5-fold in phosphate-buffered saline for automated blood cell quantification using an ADVIA 2120i hematological analyzer on the same day as harvest.

Human research ethics

Ethical approval for intestinal tissue collection from participants undergoing endoscopy procedures through the Gastroenterology Department at the Royal Melbourne Hospital was attained from the Human Research Ethics Committee (HREC): HREC 2021.074. This was in accordance with the National Health and Medical Research Council (NHMRC) National Statement on Ethical Conduct in Human Research (2008) and the Note for Guidance on Good Clinical Practice (CPMP/ICH-135/95). Site-specific governance was sought for each of the collaborating sites: WEHI and the University of Melbourne. Collaboration amongst all three participating institutions was officiated through the Melbourne Academic Centre for Health Research Collaboration Agreement (Non-Commercial). The human research in this study was performed in accordance with the principles expressed in the Helsinki Declaration. The human materials used in this study were obtained with informed consent from all subjects.

Human intestinal biopsy collection

Adult patients with or without inflammatory bowel disease (IBD) scheduled for endoscopic evaluation of the lower gastrointestinal tract (flexible sigmoidoscopy or colonoscopy) at the Gastroenterology Department at the Royal Melbourne Hospital were screened for study inclusion/exclusion. Patients were excluded based on the following criteria: active systemic (gastrointestinal and non-gastrointestinal) infection; active (solid-organ or haematological) malignancy or treatment with anti-tumour therapies; non-steroidal anti-inflammatory drug use in the last month; hereditary or familial polyposis syndromes; non-IBD forms of colitis including microscopic colitis, ischaemic colitis, diversion colitis, or diverticulitis. Eligible patients (see **Table S1**) were then consented (signed authorised Participant Information Sheet/Consent Form). For IBD patients, intestinal biopsies were retrieved endoscopically from: 1) inflamed, 2) non-inflamed, or 3) marginal areas of inflammation. The same exclusion criteria as above were applied to patients without IBD (referred to as non-IBD control patients), with biopsies retrieved endoscopically from non-inflamed segments of the intestine. Boston Scientific Radial Jaw^{TM} biopsy forceps and Olympus EVIS EXERA III endoscopes were routinely utilised for intestinal biopsy collections. Collected biopsies were immediately placed in 10% v/v Neutral Buffered Formalin. A ratio of one part tissue to >10 parts formalin was used. Tissues were incubated in formalin at room temperature for 24-72 hours before paraffin-embedding.

Blinded histopathological scoring of intestinal inflammation

Hematoxylin and eosin-stained slides from formalin-fixed paraffin-embedded biopsies were blindly scored using the Robarts Histopathology Index, a validated tool for assessing IBD activity, using previously described methodology (*118*).

Cell lines

HT29 cells were originally sourced from the American Type Culture Collection. The *RIPK1*$^{-/-}$, *RIPK3*$^{-/-}$, *MLKL*$^{-/-}$ and *CASP8*$^{-/-}$*CASP10*$^{-/-}$*MLKL*$^{-/-}$ HT29 cells have been previously reported (*68, 71, 119*) . Mouse dermal fibroblasts were generated in-house from the tails of wild-type C57BL/6J mice and immortalised by SV40 large T antigen as reported previously (*37*). The sex and precise age of these animals were not recorded, although our MDFs are routinely derived from tails from 8-week-old mice. Mouse dermal fibroblast lines were generated in accordance with protocols approved by the Walter and Eliza Hall Institute of Medical Research Animal Ethics Committee. The origin of cell lines was not further verified, although their morphologies and responses to necroptotic stimuli were consistent with their stated origins. Cell lines were monitored via polymerase chain reaction every ~6 months to confirm they were mycoplasma-free.

Cell culturing

HT29 cells and mouse dermal fibroblasts were maintained in Dulbecco's Modified Eagle Medium (DMEM; Life Technologies) with 8% v/v fetal calf serum (FCS), 2mM L-Glutamine, 50 U/mL penicillin and 50 U/mL streptomycin (G/P/S). Cells were incubated under humidified 10% CO_2 at 37^oC.

Cell treatment

HT29 cells were treated in DMEM containing 1% v/v FCS and G/P/S. Mouse dermal fibroblasts were treated in DMEM containing 8% v/v FCS and G/P/S. Media for treatment was supplemented with: 100 ng/mL recombinant human TNF-α-Fc (produced in-house as in (*120*)), 500 nM Smac mimetic/Compound A (provided by Tetralogic Pharmaceuticals as in (*121*)) 5 μM IDN-6556 (provided by Idun Pharmaceuticals). HT29 cells were treated for 7.5 hours. Mouse dermal fibroblasts were treated for 2 hours.

Cell lysate preparation

HT29 cells were homogenised in ice-cold RIPA buffer (10mM Tris-HCl pH 8.0, 1 mM EGTA, 2mM MgCl2, 0.5% v/v Triton X100, 0.1% w/v Na deoxycholate, 0.5% w/v SDS and 90mM NaCl) supplemented with 1x Protease & Phosphatase Inhibitor Cocktail (Cell Signaling Technology Cat#5872S) and 100 U/mL Benzonase (Sigma-Aldrich Cat#E1014).

Cell pellet preparation

Trypsinised cells were centrifuged at 671*g* (2000rpm) for 3 minutes at room temperature. The supernatant was discarded, cell pellets resuspended in 10% v/v Neutral Buffered Formalin, incubated for 15 minutes at room temperature, and centrifuged at 671*g* (2000rpm) for 3 minutes at room temperature. Cell pellets were resuspended in 50-70μL of HistoGel (Epredia Cat#HG-4000-012) pre-warmed to 56°C and then pipetted onto ice-cold glass coverslips to set. Set pellets were stored in 70% (v/v) ethanol until paraffin embedding.

Human tissue lysate preparation

Two intestinal biopsies (each ~1-2mm^3) were pooled, immediately washed in ice-cold DPBS (Thermo Fisher Scientific Cat#14190144) supplemented with protease inhibitors (Merck Cat#4693132001) and phosphatase inhibitors (Merck Cat#4906837001), and then homogenised with a stainless steel ball bearing in a Qiagen TissueLyzer II (30 Hz, 1min) in 0.4mL of ice-cold RIPA buffer (10mM Tris-HCl pH 8.0, 1mM EGTA, 2mM MgCl2, 0.5% v/v

Triton X100, 0.1% w/v sodium deoxycholate, 0.5% w/v SDS and 90mM NaCl) supplemented with 1x Protease & Phosphatase Inhibitor Cocktail (Cell Signaling Technology Cat#5872) and 100 U/mL Benzonase (Sigma-Aldrich Cat#E1014).

Necrosome quantitation

Necrosome detection was performed with a custom pipeline developed in Fiji (*102*). Cells were segmented using CellPose (*122*) and puncta detected using a difference-of-gaussian algorithm developed for graphics processing units (*123*). To avoid false-positives, puncta were filtered to be more than twice the signal of the average signal of the cell on which it appears. Number of cells with puncta, along with number of puncta per cell was recorded. Prior to detecting necrosomes in patient biopsies, the epithelial regions were segmented using FastPathology (v1.1.2) with a deep learning model trained on CD3-stained colon biopsy whole slide images (*124, 125*). Briefly, the whole slide images were imported into FastPathology and the default model pipeline was executed using the attribute "patch-level 4". The binary mask was imported into QuPath (v0.4.3) using the "importPyramidalTIFF.groovy" script provided at https://github.com/andreped/NoCodeSeg (*124*).

Statistical tests

The number of independent experiments and the employed statistical test for each dataset is stipulated in the respective figure legend. Statistical tests were performed using Prism v.9.5.1 (GraphPad). Statistical analyses were only performed on datasets collated from at least three independent experiments. The number of independent replicates or mice is stipulated by ‘n’, and the number of dependent replicates for each dataset is stipulated by ‘N’ in the respective figure legend.

Data Availability Statement

Customised image analysis macros used in this study are available upon request to the corresponding authors. Automated immunohistochemical staining protocols used in this study will be made available as a Supplementary File upon final publication.

List of Supplementary Materials

Fig. S1. Optimisation pipeline for the immunohistochemical detection of the mouse necroptotic pathway.

Fig. S2. Constitutive co-expression of necroptotic effectors is confined to fast-cycling cells within progenitors, immune and barrier populations.

Fig. S3. RIPK3 is uniquely upregulated in splenic germinal centres.

Fig. S4. Standardised quality control and optimisation of the immunohistochemical detection of human necroptotic proteins.

Fig. S5. Automated immunohistochemistry to detect necroptotic signaling in mouse cells.

Table S1. Patient and clinical data related to **Fig. 6**.

References and Notes:

1. S. N. Palmer, S. Chappidi, C. Pinkham, D. C. Hancks, Evolutionary Profile for (Host and Viral) MLKL Indicates Its Activities as a Battlefront for Extensive Counteradaptation. *Mol Biol Evol* **38**, 5405-5422 (2021).

2. J. W. Upton, W. J. Kaiser, E. S. Mocarski, Virus inhibition of RIP3-dependent necrosis. *Cell Host Microbe* **7**, 302-313 (2010).

3. A. Fletcher-Etherington, L. Nobre, K. Nightingale, R. Antrobus, J. Nichols, A. J. Davison, R. J. Stanton, M. P. Weekes, Human cytomegalovirus protein pUL36: A dual cell death pathway inhibitor. *Proc Natl Acad Sci U S A* **117**, 18771-18779 (2020).

4. Z. Liu, H. Nailwal, J. Rector, M. M. Rahman, R. Sam, G. McFadden, F. K. Chan, A class of viral inducer of degradation of the necroptosis adaptor RIPK3 regulates virus-induced inflammation. *Immunity* **54**, 247-258 e247 (2021).

5. J. S. Pearson, C. Giogha, S. Muhlen, U. Nachbur, C. L. Pham, Y. Zhang, J. M. Hildebrand, C. V. Oates, T. W. Lung, D. Ingle, L. F. Dagley, A. Bankovacki, E. J. Petrie, G. N. Schroeder, V. F. Crepin, G. Frankel, S. L. Masters, J. Vince, J. M. Murphy, M. Sunde, A. I. Webb, J. Silke, E. L. Hartland, EspL is a bacterial cysteine protease effector that cleaves RHIM proteins to block necroptosis and inflammation. *Nat Microbiol* **2**, 16258 (2017).

6. E. J. Petrie, J. J. Sandow, W. I. L. Lehmann, L. Y. Liang, D. Coursier, S. N. Young, W. J. A. Kersten, C. Fitzgibbon, A. L. Samson, A. V. Jacobsen, K. N. Lowes, A. E. Au, H. Jousset Sabroux, N. Lalaoui, A. I. Webb, G. Lessene, G. Manning, I. S. Lucet, J. M. Murphy, Viral MLKL Homologs Subvert Necroptotic Cell Death by Sequestering Cellular RIPK3. *Cell Rep* **28**, 3309-3319 e3305 (2019).

7. T. Zhang, C. Yin, D. F. Boyd, G. Quarato, J. P. Ingram, M. Shubina, K. B. Ragan, T. Ishizuka, J. C. Crawford, B. Tummers, D. A. Rodriguez, J. Xue, S. Peri, W. J. Kaiser, C. B. Lopez, Y. Xu, J. W. Upton, P. G. Thomas, D. R. Green, S. Balachandran, Influenza Virus Z-RNAs Induce ZBP1-Mediated Necroptosis. *Cell* **180**, 1115-1129 e1113 (2020).

8. H. W. Yeap, K. W. Chen, RIPK1 and RIPK3 in antibacterial defence. *Biochem Soc Trans* **50**, 1583-1594 (2022).

9. M. E. Choi, D. R. Price, S. W. Ryter, A. M. K. Choi, Necroptosis: a crucial pathogenic mediator of human disease. *JCI Insight* **4**, (2019).

10. Z. Fang, H. Wei, W. Gou, L. Chen, C. Bi, W. Hou, Y. Li, Recent progress in small-molecule inhibitors for critical therapeutic targets of necroptosis. *Future Med Chem* **13**, 817-837 (2021).

11. M. Devos, G. Tanghe, B. Gilbert, E. Dierick, M. Verheirstraeten, J. Nemegeer, R. de Reuver, S. Lefebvre, J. De Munck, J. Rehwinkel, P. Vandenabeele, W. Declercq, J. Maelfait, Sensing of endogenous nucleic acids by ZBP1 induces keratinocyte necroptosis and skin inflammation. *J Exp Med* **217**, (2020).

12. M. G. Naito, D. Xu, P. Amin, J. Lee, H. Wang, W. Li, M. Kelliher, M. Pasparakis, J. Yuan, Sequential activation of necroptosis and apoptosis cooperates to mediate vascular and neural pathology in stroke. *Proc Natl Acad Sci U S A* **117**, 4959-4970 (2020).

13. M. Luedde, M. Lutz, N. Carter, J. Sosna, C. Jacoby, M. Vucur, J. Gautheron, C. Roderburg, N. Borg, F. Reisinger, H. J. Hippe, A. Linkermann, M. J. Wolf, S. Rose-John, R. Lullmann-Rauch, D. Adam, U. Flogel, M. Heikenwalder, T. Luedde, N. Frey, RIP3, a kinase promoting necroptotic cell death, mediates adverse remodelling after myocardial infarction. *Cardiovasc Res* **103**, 206-216 (2014).

14. Z. Lu, H. P. Van Eeckhoutte, G. Liu, P. M. Nair, B. Jones, C. M. Gillis, B. C. Nalkurthi, F. Verhamme, T. Buyle-Huybrecht, P. Vandenabeele, T. Vanden Berghe, G. G. Brusselle, J. C. Horvat, J. M. Murphy, P. A. Wark, K. R. Bracke, M. Fricker, P. M. Hansbro, Necroptosis Signaling Promotes Inflammation, Airway Remodeling, and Emphysema in Chronic Obstructive Pulmonary Disease. *Am J Respir Crit Care Med* **204**, 667-681 (2021).

15. A. Linkermann, J. H. Brasen, M. Darding, M. K. Jin, A. B. Sanz, J. O. Heller, F. De Zen, R. Weinlich, A. Ortiz, H. Walczak, J. M. Weinberg, D. R. Green, U. Kunzendorf, S. Krautwald,

Two independent pathways of regulated necrosis mediate ischemia-reperfusion injury. *Proc Natl Acad Sci U S A* **110**, 12024-12029 (2013).

16. D. Li, L. Meng, T. Xu, Y. Su, X. Liu, Z. Zhang, X. Wang, RIPK1-RIPK3-MLKL-dependent necrosis promotes the aging of mouse male reproductive system. *Elife* **6**, (2017).

17. Y. Ito, D. Ofengeim, A. Najafov, S. Das, S. Saberi, Y. Li, J. Hitomi, H. Zhu, H. Chen, L. Mayo, J. Geng, P. Amin, J. P. DeWitt, A. K. Mookhtiar, M. Florez, A. T. Ouchida, J. B. Fan, M. Pasparakis, M. A. Kelliher, J. Ravits, J. Yuan, RIPK1 mediates axonal degeneration by promoting inflammation and necroptosis in ALS. *Science* **353**, 603-608 (2016).

18. C. Gunther, E. Martini, N. Wittkopf, K. Amann, B. Weigmann, H. Neumann, M. J. Waldner, S. M. Hedrick, S. Tenzer, M. F. Neurath, C. Becker, Caspase-8 regulates TNF-alpha-induced epithelial necroptosis and terminal ileitis. *Nature* **477**, 335-339 (2011).

19. K. Newton, D. L. Dugger, A. Maltzman, J. M. Greve, M. Hedehus, B. Martin-McNulty, R. A. Carano, T. C. Cao, N. van Bruggen, L. Bernstein, W. P. Lee, X. Wu, J. DeVoss, J. Zhang, S. Jeet, I. Peng, B. S. McKenzie, M. Roose-Girma, P. Caplazi, L. Diehl, J. D. Webster, D. Vucic, RIPK3 deficiency or catalytically inactive RIPK1 provides greater benefit than MLKL deficiency in mouse models of inflammation and tissue injury. *Cell Death Differ* **23**, 1565-1576 (2016).

20. T. Wang, N. D. Perera, M. D. F. Chiam, B. Cuic, N. Wanniarachchillage, D. Tomas, A. L. Samson, W. Cawthorne, E. N. Valor, J. M. Murphy, B. J. Turner, Necroptosis is dispensable for motor neuron degeneration in a mouse model of ALS. *Cell Death Differ* **27**, 1728-1739 (2020).

21. S. Dominguez, E. Varfolomeev, R. Brendza, K. Stark, J. Tea, J. Imperio, H. Ngu, T. Earr, O. Foreman, J. D. Webster, A. Easton, D. Vucic, B. Bingol, Genetic inactivation of RIP1 kinase does not ameliorate disease in a mouse model of ALS. *Cell Death Differ* **28**, 915-931 (2021).

22. A. Degterev, J. Hitomi, M. Germscheid, I. L. Ch'en, O. Korkina, X. Teng, D. Abbott, G. D. Cuny, C. Yuan, G. Wagner, S. M. Hedrick, S. A. Gerber, A. Lugovskoy, J. Yuan, Identification of RIP1 kinase as a specific cellular target of necrostatins. *Nat Chem Biol* **4**, 313-321 (2008).

23. S. He, L. Wang, L. Miao, T. Wang, F. Du, L. Zhao, X. Wang, Receptor interacting protein kinase-3 determines cellular necrotic response to TNF-alpha. *Cell* **137**, 1100-1111 (2009).

24. S. He, Y. Liang, F. Shao, X. Wang, Toll-like receptors activate programmed necrosis in macrophages through a receptor-interacting kinase-3-mediated pathway. *Proc Natl Acad Sci U S A* **108**, 20054-20059 (2011).

25. Y. S. Cho, S. Challa, D. Moquin, R. Genga, T. D. Ray, M. Guildford, F. K. Chan, Phosphorylation-driven assembly of the RIP1-RIP3 complex regulates programmed necrosis and virus-induced inflammation. *Cell* **137**, 1112-1123 (2009).

26. X. Chen, R. Zhu, J. Zhong, Y. Ying, W. Wang, Y. Cao, H. Cai, X. Li, J. Shuai, J. Han, Mosaic composition of RIP1-RIP3 signalling hub and its role in regulating cell death. *Nat Cell Biol*, (2022).

27. W. J. Kaiser, H. Sridharan, C. Huang, P. Mandal, J. W. Upton, P. J. Gough, C. A. Sehon, R. W. Marquis, J. Bertin, E. S. Mocarski, Toll-like receptor 3-mediated necrosis via TRIF, RIP3, and MLKL. *J Biol Chem* **288**, 31268-31279 (2013).

28. W. J. Kaiser, J. W. Upton, A. B. Long, D. Livingston-Rosanoff, L. P. Daley-Bauer, R. Hakem, T. Caspary, E. S. Mocarski, RIP3 mediates the embryonic lethality of caspase-8-deficient mice. *Nature* **471**, 368-372 (2011).

29. A. L. Samson, S. E. Garnish, J. M. Hildebrand, J. M. Murphy, Location, location, location: A compartmentalized view of TNF-induced necroptotic signaling. *Sci Signal* **14**, (2021).

30. L. Sun, H. Wang, Z. Wang, S. He, S. Chen, D. Liao, L. Wang, J. Yan, W. Liu, X. Lei, X. Wang, Mixed lineage kinase domain-like protein mediates necrosis signaling downstream of RIP3 kinase. *Cell* **148**, 213-227 (2012).

31. J. Zhao, S. Jitkaew, Z. Cai, S. Choksi, Q. Li, J. Luo, Z. G. Liu, Mixed lineage kinase domain-like is a key receptor interacting protein 3 downstream component of TNF-induced necrosis. *Proc Natl Acad Sci U S A* **109**, 5322-5327 (2012).

32. J. M. Murphy, P. E. Czabotar, J. M. Hildebrand, I. S. Lucet, J. G. Zhang, S. Alvarez-Diaz, R. Lewis, N. Lalaoui, D. Metcalf, A. I. Webb, S. N. Young, L. N. Varghese, G. M. Tannahill, E. C. Hatchell, I. J. Majewski, T. Okamoto, R. C. Dobson, D. J. Hilton, J. J. Babon, N. A. Nicola, A. Strasser, J. Silke, W. S. Alexander, The pseudokinase MLKL mediates necroptosis via a molecular switch mechanism. *Immunity* **39**, 443-453 (2013).

33. A. L. Samson, Y. Zhang, N. D. Geoghegan, X. J. Gavin, K. A. Davies, M. J. Mlodzianoski, L. W. Whitehead, D. Frank, S. E. Garnish, C. Fitzgibbon, A. Hempel, S. N. Young, A. V. Jacobsen, W. Cawthorne, E. J. Petrie, M. C. Faux, K. Shield-Artin, N. Lalaoui, J. M. Hildebrand, J. Silke, K. L. Rogers, G. Lessene, E. D. Hawkins, J. M. Murphy, MLKL trafficking and accumulation at the plasma membrane control the kinetics and threshold for necroptosis. *Nat Commun* **11**, 3151 (2020).

34. S. E. Garnish, Y. Meng, A. Koide, J. J. Sandow, E. Denbaum, A. V. Jacobsen, W. Yeung, A. L. Samson, C. R. Horne, C. Fitzgibbon, S. N. Young, P. P. C. Smith, A. I. Webb, E. J. Petrie, J. M. Hildebrand, N. Kannan, P. E. Czabotar, S. Koide, J. M. Murphy, Conformational interconversion of MLKL and disengagement from RIPK3 precede cell death by necroptosis. *Nat Commun* **12**, 2211 (2021).

35. H. Wang, L. Sun, L. Su, J. Rizo, L. Liu, L. F. Wang, F. S. Wang, X. Wang, Mixed lineage kinase domain-like protein MLKL causes necrotic membrane disruption upon phosphorylation by RIP3. *Mol Cell* **54**, 133-146 (2014).

36. X. Chen, W. Li, J. Ren, D. Huang, W. T. He, Y. Song, C. Yang, W. Li, X. Zheng, P. Chen, J. Han, Translocation of mixed lineage kinase domain-like protein to plasma membrane leads to necrotic cell death. *Cell Res* **24**, 105-121 (2014).

37. J. M. Hildebrand, M. C. Tanzer, I. S. Lucet, S. N. Young, S. K. Spall, P. Sharma, C. Pierotti, J. M. Garnier, R. C. Dobson, A. I. Webb, A. Tripaydonis, J. J. Babon, M. D. Mulcair, M. J. Scanlon, W. S. Alexander, A. F. Wilks, P. E. Czabotar, G. Lessene, J. M. Murphy, J. Silke, Activation of the pseudokinase MLKL unleashes the four-helix bundle domain to induce membrane localization and necroptotic cell death. *Proc Natl Acad Sci U S A* **111**, 15072-15077 (2014).

38. A. L. Samson, C. Fitzgibbon, K. M. Patel, J. M. Hildebrand, L. W. Whitehead, J. S. Rimes, A. V. Jacobsen, C. R. Horne, X. J. Gavin, S. N. Young, K. L. Rogers, E. D. Hawkins, J. M. Murphy, A toolbox for imaging RIPK1, RIPK3, and MLKL in mouse and human cells. *Cell Death Differ* **28**, 2126-2144 (2021).

39. J. D. Webster, M. Solon, S. Haller, K. Newton, Detection of Necroptosis by Phospho-RIPK3 Immunohistochemical Labeling. *Methods Mol Biol* **1857**, 153-160 (2018).

40. D. A. Rodriguez, R. Weinlich, S. Brown, C. Guy, P. Fitzgerald, C. P. Dillon, A. Oberst, G. Quarato, J. Low, J. G. Cripps, T. Chen, D. R. Green, Characterization of RIPK3-mediated phosphorylation of the activation loop of MLKL during necroptosis. *Cell Death Differ* **23**, 76-88 (2016).

41. C. Tabula Muris, c. Overall, c. Logistical, c. Organ, processing, p. Library, sequencing, a. Computational data, a. Cell type, g. Writing, g. Supplemental text writing, i. Principal, Single-cell transcriptomics of 20 mouse organs creates a Tabula Muris. *Nature* **562**, 367-372 (2018).

42. R. Schwarzer, H. Jiao, L. Wachsmuth, A. Tresch, M. Pasparakis, FADD and Caspase-8 Regulate Gut Homeostasis and Inflammation by Controlling MLKL- and GSDMD-Mediated Death of Intestinal Epithelial Cells. *Immunity* **52**, 978-993 e976 (2020).

43. S. M. Bader, S. P. Preston, K. Saliba, A. Lipszyc, Z. L. Grant, L. Mackiewicz, A. Baldi, A. Hempel, M. P. Clark, T. Peiris, W. Clow, J. Bjelic, M. D. Stutz, P. Arandjelovic, J. Teale, F. Du, L. Coultas, J. M. Murphy, C. C. Allison, M. Pellegrini, A. L. Samson, Endothelial Caspase-8

prevents fatal necroptotic hemorrhage caused by commensal bacteria. *Cell Death Differ* **30**, 27-36 (2023).

44. N. Tisch, C. Mogler, A. Stojanovic, R. Luck, E. A. Korhonen, A. Ellerkmann, H. Adler, M. Singhal, G. Schermann, L. Erkert, J. V. Patankar, A. Karakatsani, A. L. Scherr, Y. Fuchs, A. Cerwenka, S. Wirtz, B. C. Kohler, H. G. Augustin, C. Becker, T. Schmidt, C. Ruiz de Almodovar, Caspase-8 in endothelial cells maintains gut homeostasis and prevents small bowel inflammation in mice. *EMBO Mol Med*, e14121 (2022).

45. M. Zelic, J. E. Roderick, J. A. O'Donnell, J. Lehman, S. E. Lim, H. P. Janardhan, C. M. Trivedi, M. Pasparakis, M. A. Kelliher, RIP kinase 1-dependent endothelial necroptosis underlies systemic inflammatory response syndrome. *J Clin Invest* **128**, 2064-2075 (2018).

46. A. E. Moor, Y. Harnik, S. Ben-Moshe, E. E. Massasa, M. Rozenberg, R. Eilam, K. Bahar Halpern, S. Itzkovitz, Spatial Reconstruction of Single Enterocytes Uncovers Broad Zonation along the Intestinal Villus Axis. *Cell* **175**, 1156-1167 e1115 (2018).

47. S. Ben-Moshe, Y. Shapira, A. E. Moor, R. Manco, T. Veg, K. Bahar Halpern, S. Itzkovitz, Spatial sorting enables comprehensive characterization of liver zonation. *Nat Metab* **1**, 899-911 (2019).

48. A. L. Haber, M. Biton, N. Rogel, R. H. Herbst, K. Shekhar, C. Smillie, G. Burgin, T. M. Delorey, M. R. Howitt, Y. Katz, I. Tirosh, S. Beyaz, D. Dionne, M. Zhang, R. Raychowdhury, W. S. Garrett, O. Rozenblatt-Rosen, H. N. Shi, O. Yilmaz, R. J. Xavier, A. Regev, A single-cell survey of the small intestinal epithelium. *Nature* **551**, 333-339 (2017).

49. K. Gupta, B. Liu, PLK1-mediated S369 phosphorylation of RIPK3 during G2 and M phases enables its ripoptosome incorporation and activity. *iScience* **24**, 102320 (2021).

50. G. Liccardi, L. Ramos Garcia, T. Tenev, A. Annibaldi, A. J. Legrand, D. Robertson, R. Feltham, H. Anderton, M. Darding, N. Peltzer, M. Dannappel, H. Schunke, L. L. Fava, M. D. Haschka, T. Glatter, A. Nesvizhskii, A. Schmidt, P. A. Harris, J. Bertin, P. J. Gough, A. Villunger, J. Silke, M.

Pasparakis, K. Bianchi, P. Meier, RIPK1 and Caspase-8 Ensure Chromosome Stability Independently of Their Role in Cell Death and Inflammation. *Mol Cell* **73**, 413-428 e417 (2019).

51. M. Doerflinger, Y. Deng, P. Whitney, R. Salvamoser, S. Engel, A. J. Kueh, L. Tai, A. Bachem, E. Gressier, N. D. Geoghegan, S. Wilcox, K. L. Rogers, A. L. Garnham, M. A. Dengler, S. M. Bader, G. Ebert, J. S. Pearson, D. De Nardo, N. Wang, C. Yang, M. Pereira, C. E. Bryant, R. A. Strugnell, J. E. Vince, M. Pellegrini, A. Strasser, S. Bedoui, M. J. Herold, Flexible Usage and Interconnectivity of Diverse Cell Death Pathways Protect against Intracellular Infection. *Immunity* **53**, 533-547 e537 (2020).

52. W. D. Cook, D. M. Moujalled, T. J. Ralph, P. Lock, S. N. Young, J. M. Murphy, D. L. Vaux, RIPK1- and RIPK3-induced cell death mode is determined by target availability. *Cell Death Differ* **21**, 1600-1612 (2014).

53. L. Duprez, N. Takahashi, F. Van Hauwermeiren, B. Vandendriessche, V. Goossens, T. Vanden Berghe, W. Declercq, C. Libert, A. Cauwels, P. Vandenabeele, RIP kinase-dependent necrosis drives lethal systemic inflammatory response syndrome. *Immunity* **35**, 908-918 (2011).

54. K. Newton, D. L. Dugger, K. E. Wickliffe, N. Kapoor, M. C. de Almagro, D. Vucic, L. Komuves, R. E. Ferrando, D. M. French, J. Webster, M. Roose-Girma, S. Warming, V. M. Dixit, Activity of protein kinase RIPK3 determines whether cells die by necroptosis or apoptosis. *Science* **343**, 1357-1360 (2014).

55. P. A. Harris, S. B. Berger, J. U. Jeong, R. Nagilla, D. Bandyopadhyay, N. Campobasso, C. A. Capriotti, J. A. Cox, L. Dare, X. Dong, P. M. Eidam, J. N. Finger, S. J. Hoffman, J. Kang, V. Kasparcova, B. W. King, R. Lehr, Y. Lan, L. K. Leister, J. D. Lich, T. T. MacDonald, N. A. Miller, M. T. Ouellette, C. S. Pao, A. Rahman, M. A. Reilly, A. R. Rendina, E. J. Rivera, M. C. Schaeffer, C. A. Sehon, R. R. Singhaus, H. H. Sun, B. A. Swift, R. D. Totoritis, A. Vossenkamper, P. Ward, D. D. Wisnoski, D. Zhang, R. W. Marquis, P. J. Gough, J. Bertin,

Discovery of a First-in-Class Receptor Interacting Protein 1 (RIP1) Kinase Specific Clinical Candidate (GSK2982772) for the Treatment of Inflammatory Diseases. *J Med Chem* **60**, 1247-1261 (2017).

56. S. P. Preston, M. D. Stutz, C. C. Allison, U. Nachbur, Q. Gouil, B. M. Tran, V. Duvivier, P. Arandjelovic, J. P. Cooney, L. Mackiewicz, Y. Meng, J. Schaefer, S. M. Bader, H. Peng, Z. Valaydon, P. Rajasekaran, C. Jennison, S. Lopaticki, A. Farrell, M. Ryan, J. Howell, C. Croagh, D. Karunakaran, C. Schuster-Klein, J. M. Murphy, T. Fifis, C. Christophi, E. Vincan, M. E. Blewitt, A. Thompson, J. A. Boddey, M. Doerflinger, M. Pellegrini, Epigenetic Silencing of RIPK3 in Hepatocytes Prevents MLKL-mediated Necroptosis From Contributing to Liver Pathologies. *Gastroenterology* **163**, 1643-1657 e1614 (2022).

57. X. Li, M. Zhang, X. Huang, W. Liang, G. Li, X. Lu, Y. Li, H. Pan, L. Shi, H. Zhu, L. Qian, B. Shan, J. Yuan, Ubiquitination of RIPK1 regulates its activation mediated by TNFR1 and TLRs signaling in distinct manners. *Nat Commun* **11**, 6364 (2020).

58. Y. Xie, Y. Zhao, L. Shi, W. Li, K. Chen, M. Li, X. Chen, H. Zhang, T. Li, Y. Matsuzawa-Ishimoto, X. Yao, D. Shao, Z. Ke, J. Li, Y. Chen, X. Zhang, J. Cui, S. Cui, Q. Leng, K. Cadwell, X. Li, H. Wei, H. Zhang, H. Li, H. Xiao, Gut epithelial TSC1/mTOR controls RIPK3-dependent necroptosis in intestinal inflammation and cancer. *J Clin Invest* **130**, 2111-2128 (2020).

59. C. Gunther, B. Buchen, G. W. He, M. Hornef, N. Torow, H. Neumann, N. Wittkopf, E. Martini, M. Basic, A. Bleich, A. J. Watson, M. F. Neurath, C. Becker, Caspase-8 controls the gut response to microbial challenges by Tnf-alpha-dependent and independent pathways. *Gut* **64**, 601-610 (2015).

60. B. Wang, X. Rong, M. A. Duerr, D. J. Hermanson, P. N. Hedde, J. S. Wong, T. Q. Vallim, B. F. Cravatt, E. Gratton, D. A. Ford, P. Tontonoz, Intestinal Phospholipid Remodeling Is Required for Dietary-Lipid Uptake and Survival on a High-Fat Diet. *Cell Metab* **23**, 492-504 (2016).

61. S. Ghoshal, J. Witta, J. Zhong, W. de Villiers, E. Eckhardt, Chylomicrons promote intestinal absorption of lipopolysaccharides. *J Lipid Res* **50**, 90-97 (2009).

62. D. Gevers, S. Kugathasan, L. A. Denson, Y. Vazquez-Baeza, W. Van Treuren, B. Ren, E. Schwager, D. Knights, S. J. Song, M. Yassour, X. C. Morgan, A. D. Kostic, C. Luo, A. Gonzalez, D. McDonald, Y. Haberman, T. Walters, S. Baker, J. Rosh, M. Stephens, M. Heyman, J. Markowitz, R. Baldassano, A. Griffiths, F. Sylvester, D. Mack, S. Kim, W. Crandall, J. Hyams, C. Huttenhower, R. Knight, R. J. Xavier, The treatment-naive microbiome in new-onset Crohn's disease. *Cell Host Microbe* **15**, 382-392 (2014).

63. K. Newton, X. Sun, V. M. Dixit, Kinase RIP3 is dispensable for normal NF-kappa Bs, signaling by the B-cell and T-cell receptors, tumor necrosis factor receptor 1, and Toll-like receptors 2 and 4. *Mol Cell Biol* **24**, 1464-1469 (2004).

64. S. Alvarez-Diaz, C. P. Dillon, N. Lalaoui, M. C. Tanzer, D. A. Rodriguez, A. Lin, M. Lebois, R. Hakem, E. C. Josefsson, L. A. O'Reilly, J. Silke, W. S. Alexander, D. R. Green, A. Strasser, The Pseudokinase MLKL and the Kinase RIPK3 Have Distinct Roles in Autoimmune Disease Caused by Loss of Death-Receptor-Induced Apoptosis. *Immunity* **45**, 513-526 (2016).

65. C. R. Horne, A. L. Samson, J. M. Murphy, The web of death: the expanding complexity of necroptotic signaling. *Trends Cell Biol* **33**, 162-174 (2023).

66. M. C. Tanzer, I. Matti, J. M. Hildebrand, S. N. Young, A. Wardak, A. Tripaydonis, E. J. Petrie, A. L. Mildenhall, D. L. Vaux, J. E. Vince, P. E. Czabotar, J. Silke, J. M. Murphy, Evolutionary divergence of the necroptosis effector MLKL. *Cell Death Differ* **23**, 1185-1197 (2016).

67. K. A. Davies, C. Fitzgibbon, S. N. Young, S. E. Garnish, W. Yeung, D. Coursier, R. W. Birkinshaw, J. J. Sandow, W. I. L. Lehmann, L. Y. Liang, I. S. Lucet, J. D. Chalmers, W. M. Patrick, N. Kannan, E. J. Petrie, P. E. Czabotar, J. M. Murphy, Distinct pseudokinase domain conformations underlie divergent activation mechanisms among vertebrate MLKL orthologues. *Nat Commun* **11**, 3060 (2020).

68. E. J. Petrie, J. J. Sandow, A. V. Jacobsen, B. J. Smith, M. D. W. Griffin, I. S. Lucet, W. Dai, S. N. Young, M. C. Tanzer, A. Wardak, L. Y. Liang, A. D. Cowan, J. M. Hildebrand, W. J. A. Kersten, G. Lessene, J. Silke, P. E. Czabotar, A. I. Webb, J. M. Murphy, Conformational switching of the pseudokinase domain promotes human MLKL tetramerization and cell death by necroptosis. *Nat Commun* **9**, 2422 (2018).

69. W. Chen, Z. Zhou, L. Li, C. Q. Zhong, X. Zheng, X. Wu, Y. Zhang, H. Ma, D. Huang, W. Li, Z. Xia, J. Han, Diverse sequence determinants control human and mouse receptor interacting protein 3 (RIP3) and mixed lineage kinase domain-like (MLKL) interaction in necroptotic signaling. *J Biol Chem* **288**, 16247-16261 (2013).

70. M. L. G. Ramirez, G. S. Salvesen, A primer on caspase mechanisms. *Semin Cell Dev Biol* **82**, 79-85 (2018).

71. M. C. Tanzer, N. Khan, J. A. Rickard, N. Etemadi, N. Lalaoui, S. K. Spall, J. M. Hildebrand, D. Segal, M. Miasari, D. Chau, W. L. Wong, M. McKinlay, S. K. Chunduru, C. A. Benetatos, S. M. Condon, J. E. Vince, M. J. Herold, J. Silke, Combination of IAP antagonist and IFNgamma activates novel caspase-10- and RIPK1-dependent cell death pathways. *Cell Death Differ* **24**, 481-491 (2017).

72. T. Kobayashi, B. Siegmund, C. Le Berre, S. C. Wei, M. Ferrante, B. Shen, C. N. Bernstein, S. Danese, L. Peyrin-Biroulet, T. Hibi, Ulcerative colitis. *Nat Rev Dis Primers* **6**, 74 (2020).

73. G. Roda, S. Chien Ng, P. G. Kotze, M. Argollo, R. Panaccione, A. Spinelli, A. Kaser, L. Peyrin-Biroulet, S. Danese, Crohn's disease. *Nat Rev Dis Primers* **6**, 22 (2020).

74. D. B. Graham, R. J. Xavier, Pathway paradigms revealed from the genetics of inflammatory bowel disease. *Nature* **578**, 527-539 (2020).

75. A. N. Ananthakrishnan, Epidemiology and risk factors for IBD. *Nat Rev Gastroenterol Hepatol* **12**, 205-217 (2015).

76. R. Wang, H. Li, J. Wu, Z. Y. Cai, B. Li, H. Ni, X. Qiu, H. Chen, W. Liu, Z. H. Yang, M. Liu, J. Hu, Y. Liang, P. Lan, J. Han, W. Mo, Gut stem cell necroptosis by genome instability triggers bowel inflammation. *Nature* **580**, 386-390 (2020).

77. Y. Matsuzawa-Ishimoto, Y. Shono, L. E. Gomez, V. M. Hubbard-Lucey, M. Cammer, J. Neil, M. Z. Dewan, S. R. Lieberman, A. Lazrak, J. M. Marinis, A. Beal, P. A. Harris, J. Bertin, C. Liu, Y. Ding, M. R. M. van den Brink, K. Cadwell, Autophagy protein ATG16L1 prevents necroptosis in the intestinal epithelium. *J Exp Med* **214**, 3687-3705 (2017).

78. J. Xu, S. Li, W. Jin, H. Zhou, T. Zhong, X. Cheng, Y. Fu, P. Xiao, H. Cheng, D. Wang, Y. Ke, Z. Jiang, X. Zhang, Epithelial Gab1 calibrates RIPK3-dependent necroptosis to prevent intestinal inflammation. *JCI Insight* **8**, (2023).

79. K. Vlantis, A. Wullaert, A. Polykratis, V. Kondylis, M. Dannappel, R. Schwarzer, P. Welz, T. Corona, H. Walczak, F. Weih, U. Klein, M. Kelliher, M. Pasparakis, NEMO Prevents RIP Kinase 1-Mediated Epithelial Cell Death and Chronic Intestinal Inflammation by NF-kappaB-Dependent and -Independent Functions. *Immunity* **44**, 553-567 (2016).

80. M. Pierdomenico, A. Negroni, L. Stronati, R. Vitali, E. Prete, J. Bertin, P. J. Gough, M. Aloi, S. Cucchiara, Necroptosis is active in children with inflammatory bowel disease and contributes to heighten intestinal inflammation. *Am J Gastroenterol* **109**, 279-287 (2014).

81. A. Negroni, E. Colantoni, M. Pierdomenico, F. Palone, M. Costanzo, S. Oliva, A. Tiberti, S. Cucchiara, L. Stronati, RIP3 AND pMLKL promote necroptosis-induced inflammation and alter membrane permeability in intestinal epithelial cells. *Dig Liver Dis* **49**, 1201-1210 (2017).

82. Y. Shi, X. Cui, Y. Sun, Q. Zhao, T. Liu, Intestinal vitamin D receptor signaling ameliorates dextran sulfate sodium-induced colitis by suppressing necroptosis of intestinal epithelial cells. *FASEB J* **34**, 13494-13506 (2020).

83. K. Weisel, N. Scott, S. Berger, S. Wang, K. Brown, M. Powell, M. Broer, C. Watts, D. J. Tompson, S. W. Burriss, S. Hawkins, K. Abbott-Banner, P. P. Tak, A randomised, placebo-controlled study of RIPK1 inhibitor GSK2982772 in patients with active ulcerative colitis. *BMJ Open Gastroenterol* **8**, (2021).

84. T. Geiger, A. Velic, B. Macek, E. Lundberg, C. Kampf, N. Nagaraj, M. Uhlen, J. Cox, M. Mann, Initial quantitative proteomic map of 28 mouse tissues using the SILAC mouse. *Mol Cell Proteomics* **12**, 1709-1722 (2013).

85. M. N. Bobrow, P. T. Moen, Jr., Tyramide signal amplification (TSA) systems for the enhancement of ISH signals in cytogenetics. *Curr Protoc Cytom* **Chapter 8**, Unit 8 9 (2001).

86. G. Landini, G. Martinelli, F. Piccinini, Colour deconvolution: stain unmixing in histological imaging. *Bioinformatics* **37**, 1485-1487 (2021).

87. L. Li, K. Huang, C. Ruan, J. Han, Y. Zhang, Immunostaining of phospho-RIPK3 in L929 cells, murine yolk sacs, ceca, and small intestines. *STAR Protoc* **3**, 101517 (2022).

88. P. He, T. Ai, Z. H. Yang, J. Wu, J. Han, Detection of necroptosis by phospho-MLKL immunohistochemical labeling. *STAR Protoc* **2**, 100251 (2021).

89. D. A. Rodriguez, G. Quarato, S. Liedmann, B. Tummers, T. Zhang, C. Guy, J. C. Crawford, G. Palacios, S. Pelletier, H. Kalkavan, J. J. P. Shaw, P. Fitzgerald, M. J. Chen, S. Balachandran, D. R. Green, Caspase-8 and FADD prevent spontaneous ZBP1 expression and necroptosis. *Proc Natl Acad Sci U S A* **119**, e2207240119 (2022).

90. J. M. Hildebrand, M. Kauppi, I. J. Majewski, Z. Liu, A. J. Cox, S. Miyake, E. J. Petrie, M. A. Silk, Z. Li, M. C. Tanzer, G. Brumatti, S. N. Young, C. Hall, S. E. Garnish, J. Corbin, M. D. Stutz, L. Di Rago, P. Gangatirkar, E. C. Josefsson, K. Rigbye, H. Anderton, J. A. Rickard, A. Tripaydonis, J. Sheridan, T. S. Scerri, V. E. Jackson, P. E. Czabotar, J. G. Zhang, L. Varghese, C. C. Allison, M. Pellegrini, G. M. Tannahill, E. C. Hatchell, T. A. Willson, D. Stockwell, C. A. de Graaf, J. Collinge, A. Hilton, N. Silke, S. K. Spall, D. Chau, V. Athanasopoulos, D. Metcalf, R. M. Laxer,

A. G. Bassuk, B. W. Darbro, M. A. Fiatarone Singh, N. Vlahovich, D. Hughes, M. Kozlovskaia, D. B. Ascher, K. Warnatz, N. Venhoff, J. Thiel, C. Biben, S. Blum, J. Reveille, M. S. Hildebrand, C. G. Vinuesa, P. McCombe, M. A. Brown, B. T. Kile, C. McLean, M. Bahlo, S. L. Masters, H. Nakano, P. J. Ferguson, J. M. Murphy, W. S. Alexander, J. Silke, A missense mutation in the MLKL brace region promotes lethal neonatal inflammation and hematopoietic dysfunction. *Nat Commun* **11**, 3150 (2020).

91. S. E. Garnish, K. R. Martin, M. Kauppi, V. E. Jackson, R. Ambrose, V. V. Eng, S. Chiou, Y. Meng, D. Frank, E. C. Tovey Crutchfield, K. M. Patel, A. V. Jacobsen, G. K. Atkin-Smith, L. Di Rago, M. Doerflinger, C. R. Horne, C. Hall, S. N. Young, M. Cook, V. Athanasopoulos, C. G. Vinuesa, K. E. Lawlor, I. P. Wicks, G. Ebert, A. P. Ng, C. A. Slade, J. S. Pearson, A. L. Samson, J. Silke, J. M. Murphy, J. M. Hildebrand, A common human MLKL polymorphism confers resistance to negative regulation by phosphorylation. *Nat Commun* **14**, 6046 (2023).

92. X. Zhu, N. Yang, Y. Yang, F. Yuan, D. Yu, Y. Zhang, Z. Shu, N. Nan, H. Hu, X. Liu, S. Chen, L. Sun, H. Wang, Spontaneous necroptosis and autoinflammation are blocked by an inhibitory phosphorylation on MLKL during neonatal development. *Cell Res* **32**, 407-410 (2022).

93. M. Vucur, A. Ghallab, A. T. Schneider, A. Adili, M. Cheng, M. Castoldi, M. T. Singer, V. Buttner, L. S. Keysberg, L. Kusgens, M. Kohlhepp, B. Gorg, S. Gallage, J. E. Barragan Avila, K. Unger, C. Kordes, A. L. Leblond, W. Albrecht, S. H. Loosen, C. Lohr, M. S. Jordens, A. Babler, S. Hayat, D. Schumacher, M. T. Koenen, O. Govaere, M. V. Boekschoten, S. Jors, C. Villacorta-Martin, V. Mazzaferro, J. M. Llovet, R. Weiskirchen, J. N. Kather, P. Starlinger, M. Trauner, M. Luedde, L. R. Heij, U. P. Neumann, V. Keitel, J. G. Bode, R. K. Schneider, F. Tacke, B. Levkau, T. Lammers, G. Fluegen, T. Alexandrov, A. L. Collins, G. Nelson, F. Oakley, D. A. Mann, C. Roderburg, T. Longerich, A. Weber, A. Villanueva, A. L. Samson, J. M. Murphy, R. Kramann, F. Geisler, I. G. Costa, J. G. Hengstler, M. Heikenwalder, T. Luedde, Sublethal necroptosis signaling promotes inflammation and liver cancer. *Immunity* **56**, 1578-1595 e1578 (2023).

94. A. Degterev, Z. Huang, M. Boyce, Y. Li, P. Jagtap, N. Mizushima, G. D. Cuny, T. J. Mitchison, M. A. Moskowitz, J. Yuan, Chemical inhibitor of nonapoptotic cell death with therapeutic potential for ischemic brain injury. *Nat Chem Biol* **1**, 112-119 (2005).

95. M. Uhlen, L. Fagerberg, B. M. Hallstrom, C. Lindskog, P. Oksvold, A. Mardinoglu, A. Sivertsson, C. Kampf, E. Sjostedt, A. Asplund, I. Olsson, K. Edlund, E. Lundberg, S. Navani, C. A. Szigyarto, J. Odeberg, D. Djureinovic, J. O. Takanen, S. Hober, T. Alm, P. H. Edqvist, H. Berling, H. Tegel, J. Mulder, J. Rockberg, P. Nilsson, J. M. Schwenk, M. Hamsten, K. von Feilitzen, M. Forsberg, L. Persson, F. Johansson, M. Zwahlen, G. von Heijne, J. Nielsen, F. Ponten, Proteomics. Tissue-based map of the human proteome. *Science* **347**, 1260419 (2015).

96. L. A. O'Reilly, U. Divisekera, K. Newton, K. Scalzo, T. Kataoka, H. Puthalakath, M. Ito, D. C. Huang, A. Strasser, Modifications and intracellular trafficking of FADD/MORT1 and caspase-8 after stimulation of T lymphocytes. *Cell Death Differ* **11**, 724-736 (2004).

97. N. Percie du Sert, V. Hurst, A. Ahluwalia, S. Alam, M. T. Avey, M. Baker, W. J. Browne, A. Clark, I. C. Cuthill, U. Dirnagl, M. Emerson, P. Garner, S. T. Holgate, D. W. Howells, N. A. Karp, S. E. Lazic, K. Lidster, C. J. MacCallum, M. Macleod, E. J. Pearl, O. H. Petersen, F. Rawle, P. Reynolds, K. Rooney, E. S. Sena, S. D. Silberberg, T. Steckler, H. Wurbel, The ARRIVE guidelines 2.0: Updated guidelines for reporting animal research. *PLoS Biol* **18**, e3000410 (2020).

98. E. C. Tovey Crutchfield, S. E. Garnish, J. Day, H. Anderton, S. Chiou, A. Hempel, C. Hall, K. M. Patel, P. Gangatirkar, K. R. Martin, C. S. N. Li Wai Suen, A. L. Garnham, A. J. Kueh, I. P. Wicks, J. Silke, U. Nachbur, A. L. Samson, J. M. Murphy, J. M. Hildebrand, MLKL deficiency protects against low-grade, sterile inflammation in aged mice. *Cell Death Differ* **30**, 1059-1071 (2023).

99. J. A. Rickard, J. A. O'Donnell, J. M. Evans, N. Lalaoui, A. R. Poh, T. Rogers, J. E. Vince, K. E. Lawlor, R. L. Ninnis, H. Anderton, C. Hall, S. K. Spall, T. J. Phesse, H. E. Abud, L. H. Cengia, J. Corbin, S. Mifsud, L. Di Rago, D. Metcalf, M. Ernst, G. Dewson, A. W. Roberts, W. S. Alexander, J. M. Murphy, P. G. Ekert, S. L. Masters, D. L. Vaux, B. A. Croker, M. Gerlic, J. Silke, RIPK1 regulates RIPK3-MLKL-driven systemic inflammation and emergency hematopoiesis. *Cell* **157**, 1175-1188 (2014).

100. M. A. Kelliher, S. Grimm, Y. Ishida, F. Kuo, B. Z. Stanger, P. Leder, The death domain kinase RIP mediates the TNF-induced NF-kappaB signal. *Immunity* **8**, 297-303 (1998).

101. L. Salmena, B. Lemmers, A. Hakem, E. Matysiak-Zablocki, K. Murakami, P. Y. Au, D. M. Berry, L. Tamblyn, A. Shehabeldin, E. Migon, A. Wakeham, D. Bouchard, W. C. Yeh, J. C. McGlade, P. S. Ohashi, R. Hakem, Essential role for caspase 8 in T-cell homeostasis and T-cell-mediated immunity. *Genes Dev* **17**, 883-895 (2003).

102. J. Schindelin, I. Arganda-Carreras, E. Frise, V. Kaynig, M. Longair, T. Pietzsch, S. Preibisch, C. Rueden, S. Saalfeld, B. Schmid, J. Y. Tinevez, D. J. White, V. Hartenstein, K. Eliceiri, P. Tomancak, A. Cardona, Fiji: an open-source platform for biological-image analysis. *Nat Methods* **9**, 676-682 (2012).

103. Y. Hao, S. Hao, E. Andersen-Nissen, W. M. Mauck, 3rd, S. Zheng, A. Butler, M. J. Lee, A. J. Wilk, C. Darby, M. Zager, P. Hoffman, M. Stoeckius, E. Papalexi, E. P. Mimitou, J. Jain, A. Srivastava, T. Stuart, L. M. Fleming, B. Yeung, A. J. Rogers, J. M. McElrath, C. A. Blish, R. Gottardo, P. Smibert, R. Satija, Integrated analysis of multimodal single-cell data. *Cell* **184**, 3573-3587 e3529 (2021).

104. T. Stuart, A. Butler, P. Hoffman, C. Hafemeister, E. Papalexi, W. M. Mauck, 3rd, Y. Hao, M. Stoeckius, P. Smibert, R. Satija, Comprehensive Integration of Single-Cell Data. *Cell* **177**, 1888-1902 e1821 (2019).

105. A. Butler, P. Hoffman, P. Smibert, E. Papalexi, R. Satija, Integrating single-cell transcriptomic data across different conditions, technologies, and species. *Nat Biotechnol* **36**, 411-420 (2018).

106. R. Satija, J. A. Farrell, D. Gennert, A. F. Schier, A. Regev, Spatial reconstruction of single-cell gene expression data. *Nat Biotechnol* **33**, 495-502 (2015).

107. A. Ly, Y. Liao, H. Pietrzak, L. J. Ioannidis, T. Sidwell, R. Gloury, M. Doerflinger, T. Triglia, R. Z. Qin, J. R. Groom, G. T. Belz, K. L. Good-Jacobson, W. Shi, A. Kallies, D. S. Hansen, Transcription Factor T-bet in B Cells Modulates Germinal Center Polarization and Antibody Affinity Maturation in Response to Malaria. *Cell Rep* **29**, 2257-2269 e2256 (2019).

108. A. Chen, S. Liao, M. Cheng, K. Ma, L. Wu, Y. Lai, X. Qiu, J. Yang, J. Xu, S. Hao, X. Wang, H. Lu, X. Chen, X. Liu, X. Huang, Z. Li, Y. Hong, Y. Jiang, J. Peng, S. Liu, M. Shen, C. Liu, Q. Li, Y. Yuan, X. Wei, H. Zheng, W. Feng, Z. Wang, Y. Liu, Z. Wang, Y. Yang, H. Xiang, L. Han, B. Qin, P. Guo, G. Lai, P. Munoz-Canoves, P. H. Maxwell, J. P. Thiery, Q. F. Wu, F. Zhao, B. Chen, M. Li, X. Dai, S. Wang, H. Kuang, J. Hui, L. Wang, J. F. Fei, O. Wang, X. Wei, H. Lu, B. Wang, S. Liu, Y. Gu, M. Ni, W. Zhang, F. Mu, Y. Yin, H. Yang, M. Lisby, R. J. Cornall, J. Mulder, M. Uhlen, M. A. Esteban, Y. Li, L. Liu, X. Xu, J. Wang, Spatiotemporal transcriptomic atlas of mouse organogenesis using DNA nanoball-patterned arrays. *Cell* **185**, 1777-1792 e1721 (2022).

109. M. Martin, Cutadapt removes adapter sequences from high-throughput sequencing reads. *2011* **17**, 3 (2011).

110. D. Kim, J. M. Paggi, C. Park, C. Bennett, S. L. Salzberg, Graph-based genome alignment and genotyping with HISAT2 and HISAT-genotype. *Nat Biotechnol* **37**, 907-915 (2019).

111. Y. Liao, G. K. Smyth, W. Shi, featureCounts: an efficient general purpose program for assigning sequence reads to genomic features. *Bioinformatics* **30**, 923-930 (2014).

112. Y. Liao, G. K. Smyth, W. Shi, The R package Rsubread is easier, faster, cheaper and better for alignment and quantification of RNA sequencing reads. *Nucleic Acids Res* **47**, e47 (2019).

113. M. D. Robinson, A. Oshlack, A scaling normalization method for differential expression analysis of RNA-seq data. *Genome Biol* **11**, R25 (2010).

114. C. W. Law, Y. Chen, W. Shi, G. K. Smyth, voom: Precision weights unlock linear model analysis tools for RNA-seq read counts. *Genome Biol* **15**, R29 (2014).

115. Y. Benjamini, Y. Hochberg, Controlling the False Discovery Rate: A Practical and Powerful Approach to Multiple Testing. *Journal of the Royal Statistical Society: Series B (Methodological)* **57**, 289-300 (1995).

116. I. Y. Kong, S. Trezise, A. Light, I. Todorovski, G. M. Arnau, S. Gadipally, D. Yoannidis, K. J. Simpson, X. Dong, L. Whitehead, J. C. Tempany, A. J. Farchione, A. A. Sheikh, J. R. Groom, K. L. Rogers, M. J. Herold, V. L. Bryant, M. E. Ritchie, S. N. Willis, R. W. Johnstone, P. D. Hodgkin, S. L. Nutt, S. J. Vervoort, E. D. Hawkins, Epigenetic modulators of B cell fate identified through coupled phenotype-transcriptome analysis. *Cell Death Differ* **29**, 2519-2530 (2022).

117. K. G. Smith, A. Light, L. A. O'Reilly, S. M. Ang, A. Strasser, D. Tarlinton, bcl-2 transgene expression inhibits apoptosis in the germinal center and reveals differences in the selection of memory B cells and bone marrow antibody-forming cells. *J Exp Med* **191**, 475-484 (2000).

118. M. H. Mosli, B. G. Feagan, G. Zou, W. J. Sandborn, G. D'Haens, R. Khanna, L. M. Shackelton, C. W. Walker, S. Nelson, M. K. Vandervoort, V. Frisbie, M. A. Samaan, V. Jairath, D. K. Driman, K. Geboes, M. A. Valasek, R. K. Pai, G. Y. Lauwers, R. Riddell, L. W. Stitt, B. G. Levesque, Development and validation of a histological index for UC. *Gut* **66**, 50-58 (2017).

119. A. V. Jacobsen, C. L. Pierotti, K. N. Lowes, A. E. Au, Y. Zhang, N. Etemadi, C. Fitzgibbon, W. J. A. Kersten, A. L. Samson, M. F. van Delft, D. C. S. Huang, H. J. Sabroux, G. Lessene, J. Silke, J. M. Murphy, The Lck inhibitor, AMG-47a, blocks necroptosis and implicates RIPK1 in signalling downstream of MLKL. *Cell Death Dis* **13**, 291 (2022).

120. C. Bossen, K. Ingold, A. Tardivel, J. L. Bodmer, O. Gaide, S. Hertig, C. Ambrose, J. Tschopp, P. Schneider, Interactions of tumor necrosis factor (TNF) and TNF receptor family members in the mouse and human. *J Biol Chem* **281**, 13964-13971 (2006).

121. J. E. Vince, W. W. Wong, N. Khan, R. Feltham, D. Chau, A. U. Ahmed, C. A. Benetatos, S. K. Chunduru, S. M. Condon, M. McKinlay, R. Brink, M. Leverkus, V. Tergaonkar, P. Schneider, B. A. Callus, F. Koentgen, D. L. Vaux, J. Silke, IAP antagonists target cIAP1 to induce TNFalpha-dependent apoptosis. *Cell* **131**, 682-693 (2007).

122. C. Stringer, T. Wang, M. Michaelos, M. Pachitariu, Cellpose: a generalist algorithm for cellular segmentation. *Nat Methods* **18**, 100-106 (2021).

123. R. Haase, L. A. Royer, P. Steinbach, D. Schmidt, A. Dibrov, U. Schmidt, M. Weigert, N. Maghelli, P. Tomancak, F. Jug, E. W. Myers, CLIJ: GPU-accelerated image processing for everyone. *Nat Methods* **17**, 5-6 (2020).

124. A. Pedersen, A. Valla, M. Bofin, J. P. De Frutos, I. Reinersten, E. Smistad, FastPathology: An Open-Source Platform for Deep Learning-Based Research and Decision Support in Digital Pathology. *IEEE Access* **9**, 58216-58229 (2021).

125. H. S. Pettersen, I. Belevich, E. S. Royset, E. Smistad, M. R. Simpson, E. Jokitalo, I. Reinertsen, I. Bakke, A. Pedersen, Code-Free Development and Deployment of Deep Segmentation Models for Digital Pathology. *Front Med (Lausanne)* **8**, 816281 (2021).

Acknowledgements:

We thanks James Vince, Jiyi Pang, David Tarlington, Angus Stock, Najoua Lalaoui, Asha Jois, Marcel Doerflinger, Quentin Gouil and Bruce Rosengarten for constructive feedback and reagents during the preparation of this manuscript. We thank WEHI Monoclonal antibody facility for producing several antibodies used in this study. We thank the WEHI Histology team for high level support with immunohistochemistry. We thank the WEHI Bioservices team for high level support for animal experimentation, welfare, and ethics. We thank Kim Newton and Vishva Dixit for sharing the *Ripk3*$^{-/-}$ mice that were used to make the *Casp8*$^{-/-}$*Ripk3*$^{-/-}$ mice, and thank Michelle Kelliher for the *Ripk1*$^{-/-}$ mice that were used to generate the *Casp8*$^{-/-}$*Ripk1*$^{-/-}$*Ripk3-/-* mice. We are grateful to the Department of Gastroenterology at the Royal Melbourne Hospital for performing endoscopies and to the patients who consented to donating their material to be used in this study.

Funding

This work was supported by National Health and Medical Research Council of Australia (grants 1172929 to JMM, 2008652 to EDH, 2002965 to ALS, and the Independent Research Institutes Infrastructure Support Scheme 9000719), by the Kenneth Rainin Foundation (award to JMM, BC, AHA, ALS), and by the Victorian State Government Operational Infrastructure Support scheme. SC is supported by the WEHI Handman PhD scholarship, and AHA by the Avant Foundation and by Crohn’s and Colitis Australia. JMM and JS received research funding from Anaxis Pharma Pty Ltd, from which the salaries of KMP, AH, AL and PG were paid.

Competing interests

KMP, SNY, AH, AL, PG, CRH, JD, IPW, JMH, JS, JMM and ALS have contributed to the development of necroptosis pathway inhibitors in collaboration with Anaxis Pharma Pty Ltd. All other authors have no additional financial interests.

Author contributions

Data collection and experimental assistance: SC, AHA, YP, KMP, AL, SNY, MB, LZ, AH, AL, CH, PG, WC, JMH, ET, ALS. Data analysis and interpretation: SC, AHA, YP, LWW, IYK, AL, CS, RKHY, PR, JAR, JMH, EDH, BC, JMM, ALS. Conceptualization: JMM, ALS. Essential reagents: CH, AVJ, CRH, DSH, LJI, JD, IPW, LAO, JS, EDH, JMM. Manuscript writing: SC, AHA, JMM, ALS. Reagents, supervision, and infrastructure: DH, IPW, CL, MER, RB, LAO, JS, LG-R, ET, KLR, EDH, BC, JMM, ALS.

Abbreviations

C8 (Caspase-8), C10 (Caspase-10), cl. C3 (cleaved Caspase-3), TNF (Tumour Necrosis Factor), RIPK1 (Receptor-interacting serine/threonine-protein kinase-1), pRIPK1 (phosphorylated RIPK1), RIPK3 (Receptor-interacting serine/threonine-protein kinase-3), pRIPK3 (phosphorylated RIPK3), MLKL (Mixed lineage kinase domain-like protein), pMLKL (phosphorylated MLKL), R1 (Receptor-interacting serine/threonine-protein kinase-1), R3 (Receptor-interacting serine/threonine-protein kinase-1), ML (Mixed lineage kinase domain-like protein), WEHI (Walter and Eliza Hall Institute of Medical Research), WT (wild-type), KO (knockout), IBD (inflammatory bowel disease), UC (ulcerative colitis), CD (Crohn’s disease), SMA (smooth muscle actin), Kpf (Kupffer cell), endo (endothelial cell), p.o. (oral administration), i.p. (intraperitoneal administration), CV (central vein), PV (portal vein), BD (bile duct), CA (splenic central artery), WP (splenic white pulp), MZ (splenic marginal zone), RP (splenic red pulp), CRP (C-reactive protein), TS (Tumour Necrosis Factor and SMAC mimetic), TSI (Tumour Necrosis Factor and SMAC mimetic and IDN-6556), Ab (antibody), Uniform Manifold Approximation and Projection (UMAP), NP-KLH (4-hydroxy-3-nitrophenylacetyl hapten conjugated to keyhole limpet hemocyanin).

Figure legends:

Fig. 1. Automated immunohistochemistry shows constitutive necroptotic pathway expression is restricted. **A** To gauge immunohistochemistry performance, immunosignals from wild-type (WT) versus knockout (KO) tissue were deconvoluted, (i) pixel intensities plotted, (ii) ratioed to yield a signal-to-noise (S/N) histogram, and then (iv) integrated. **B** Heatmap shows relative integrated S/N values from 7 automated immunohistochemistry protocols across 7 tissues. Column headers indicate the antibody target clone name. Data are representative of n≥3 for each target and tissue. **C** Heatmap depicts relative protein abundance values as measured by (*84*). **D** Immunosignals of Caspase-8, RIPK1, RIPK3 and MLKL in wild-type versus the appropriate knockout (KO) tissue from *Mlkl*$^{-/-}$ or *Casp8*$^{-/-}$*Ripk3*$^{-/-}$ or *Casp8*$^{-/-}$*Ripk1*$^{-/-}$*Ripk3*$^{-/-}$. Data are representative of n≥3 for each target and tissue. Scale bars are 500µm. Related to **Fig. S1**.

Fig. 2. Necroptotic potential is spatially graded across tissue zones. **A** Immunosignals of Caspase-8, RIPK1 and RIPK3 from wild-type mouse ileum (i), colon (ii), liver (iii) and spleen (iv). The crypt base (crypt), villi/crypt tip (tip), central vein (CV), portal vein (PV), bile duct (BD), central artery (CA), white pulp (WP), marginal zone (MZ) and red pulp (RP) are annotated. Inset of immunostaining in the ileum shows lower RIPK3 expression in Paneth cells (open arrowhead) relative to neighbouring cells. Arrow shows peri-central hepatocytes that express higher levels of Caspase-8. Closed arrowheads show Caspase-8^{+} RIPK1^{+} RIPK3^{+} Kupffer cells. Scale bars are 50µm, except for 10µm scale bar in inset. Data are representative of n≥3 for each target and tissue. **B** Relative expression levels of Caspase-8, RIPK1, RIPK3 (and splenic MLKL; **Fig. S2B**) along the indicated tissue axes. Red datapoints indicate immunosignal intensities, and the overlaid dark blue line indicating the LOWESS best-fit along N=20 axes per tissue. Best-fit curves are superimposed in the left-most column. Dashed line indicates the boundary between splenic white pulp and marginal zone. Data are representative of n>3 mice per target per

tissue. **C** Scatterplots where each dot represents a different cell ontology from the *Tabula Muris* dataset *(41)*. The percent of cells within each ontology that expressed *Mki67*, *Ripk1* or *Ripk3* was plotted against that of *Top2a*. Pearson correlation coefficient values are shown. Related to **Fig. S2**.

Fig. 3. RIPK3 expression is rapidly altered during systemic inflammation. A Experimental design. **B** Core temperatures of vehicle- and TNF-injected mice (n=3 mice per group). **C** Immunosignals for cleaved Caspase-3 (cl. C3), Caspase-8, RIPK1 or RIPK3 from the spleen of vehicle- or TNF-injected mice. Insets show unidentified RIPK1^{high} cells that associate with apoptotic bodies in splenic white pulp. **D** Graph of white pulp area occupied by cleaved Caspase-3^{+} material in vehicle- and TNF-treated mice. Each red datapoint represents one white pulp lobule (N=20 lobules/mouse). Blue datapoints indicate the median value per mouse (n=3 mice/treatment). Black bars represent the mean value per group. *p<0.05 by unpaired 2-tailed t-test. **E** RIPK3 immunosignals in colon of vehicle- or TNF-treated mice. **F** Best-fit curves of RIPK3 immunosignals along the crypt-to-tip axis from N=10 axes per mouse (n=3 mice/group). ***p<0.001 by multiple unpaired 2-tailed t-test. **G** RIPK3 (pink) and smooth muscle actin (brown) immunosignals in intestinal submucosa of vehicle- or TNF-treated mice. Insets show vessel cross-sections. Arrowheads show RIPK3^{+} endothelial cells (endo). **H** Plot of RIPK3 signals per vessel. Each red datapoint represents one vessel (N=50 vessels/mouse). Blue datapoints indicate the median value per mouse (n=3 mice/treatment). Black bars represent the mean value per group. *p<0.05 by unpaired 2-tailed t-test. **I** RIPK3 immunosignals in liver of vehicle- or TNF-treated mice. Central vein (CV), portal vein (PV) and Kupffer cell (Kpf). **J** Plot of RIPK3 signals per hepatocyte or Kupffer cell. Each transparent datapoint represents one cell (N=90 cells/mouse). Opaque datapoints indicate the median value per mouse (n=3

mice/treatment). Black bars represent the mean value per group. *p<0.05 and **p<0.01 by unpaired 2-tailed t-test.

Fig. 4. RIPK3 expression changes in response to dysbiosis. **A** Experimental design. **B** Bulk RNA sequencing was performed on indicated tissues. Heatmap depicts the log fold-change in gene expression for antibiotic- versus water-treated mice. Each row represents a different mouse. Legend shows the colour-to-value scale. **C** Immunoblots for the indicated proteins in the ileum and spleen of water- versus antibiotic-treated mice. Arrowheads indicate full-length proteins of interest. Coomassie staining of total protein content was used as a loading control. Data are representative of n=3 mice per tissue per group. **D** Caspase-8, RIPK3 and RIPK3 immunosignals in the ileum of water- or antibiotic-treated mice. Arrowheads to cytosolic accumulations of RIPK1 and RIPK3 in epithelial cells at villi tips. Scale bars in lower magnification micrographs are 100µm. Scale bars in insets are 10µm. Data are representative of n=3 mice per group.

Fig. 5. Automated immunohistochemistry quantifies necroptotic signaling in human cells. **A** Immunosignals of cleaved Caspase-3, Caspase-8, RIPK1 and MLKL in wild-type versus *MLKL*$^{-/-}$ or *RIPK1*$^{-/-}$ or *CASP8*$^{-/-}$*CASP10*$^{-/-}$*MLKL*$^{-/-}$ HT29 cells. Arrowheads indicate Caspase-8^{+}, RIPK1^{+} and MLKL^{+} puncta that are presumed to be necrosomes. Data are representative of n≥2 for each protein and treatment. Scale bars in lower magnification micrographs are 10µm. Scale bars in insets are 2µm. **B** The percent of cells per treatment group that contain cytosolic necrosome-like puncta immunostained by the stipulated antibody. N=1051-5630 cells were analysed per condition per stain. Data representative of n=2 experiments. **C** The number of puncta per cell. N=1000 cells per treatment group were analysed. Each datapoint represents one cell. Black bar indicates mean value.

****p<0.0001 by one-way ANOVA with Krukal-Wallis post-hoc correction. Data representative of n=2 experiments. Related to **Fig. S4** and **S5**.

Fig. 6. Case study for the detection of necroptotic signaling in inflammatory bowel disease. A Study design. **B** Blinded histopathological (RHI) scores of disease activity in intestinal biopsies relative to their endoscopic grading of inflammation. Diamond indicates a sample that could not be formally scored, as it was solely comprised of neutrophilic exudate, but was given a pseudo-score of 15 that likely underrepresents the extend of disease activity in this biopsy. Biopsies scored in Panel B were matched to those used in Panels C-E (see **Table S1** for details). **C** Immunoblot of lysates from treated HT29 cells (red annotations) and intestinal biopsies from patients A-H (blue annotations). The fifth lane of each gel contained lysates from TSI-treated *RIPK3*$^{-/-}$ or TSI-treated *MLKL*$^{-/-}$ cells (see source data for details). Patients A,C,E,G were non-IBD controls. Patients B and D had ulcerative colitis (UC). Patients F and H had Crohn's disease (CD). The endoscopic grading of the biopsy site as 'non-inflamed', 'marginally inflamed' or 'inflamed' is stipulated. Closed arrowheads indicate full-length form of proteins. Asterisks indicate active, phosphorylated forms of RIPK3 (pRIPK3) and MLKL (pMLKL). Open arrowheads indicate active, cleaved forms of Caspase-8, Caspase-10 and Caspase-3. GAPDH was used as a loading control. **D** Immunohistochemistry for Caspase-8 on intestinal biopsies. Insets a-e show diffuse epithelial Caspase-8 in patient C. Insets f-j show mild clustering of epithelial Caspase-8 and insets k-o show more pronounced clustering of epithelial Caspase-8 in patient D (arrowheads). Scale bars in lower magnification micrographs are 500µm. Scale bars in insets are 10µm. **E** The number of Caspase-8^{+} puncta per 100 cells. Each datapoint represents one crypt. Whole slide scans with N=20246 cells from the 'non-IBD patient C' biopsy, N=10416 cells from the 'non-inflamed patient D' biopsy, and N=30799

cells from the 'inflamed patient D' biopsy were analysed. Black bar indicates mean value. **p<0.01 by one-way ANOVA with Tukey's post-hoc correction.

Supplementary Materials:

Fig. S1. Optimisation pipeline for the immunohistochemical detection of the mouse necroptotic pathway. Summary of the steps used to test the specificity and to optimise the immunohistochemistry performance of monoclonal antibodies against mouse MLKL, RIPK3, RIPK1 and Caspase-8. Step 1: Immunoblot signals for each antibody on spleen homogenates from wild-type mice (WT) and *Mlkl*$^{-/-}$ or *Casp8*$^{-/-}$*Ripk3*$^{-/-}$ or *Casp8*$^{-/-}$*Ripk1*$^{-/-}$ *Ripk3*$^{-/-}$ mice (KO). Arrowheads indicate the full-length protein of interest. Representative GAPDH immunoblots are shown as loading controls. Data are representative of n=1-2 immunoblots per antibody. Steps 2-4: Heatmaps depict the integrated signal-to-noise values derived from immunohistochemical signals for each antibody on WT versus KO spleen sections. Legend shows the heatmap color-to-value scale. Step 2 varied the primary antibody concentration and the antigen retrieval pH. Step 3 varied the blocking reagent and the antigen retrieval time. Step 4 varied the amplification technique, amplification time, peroxidase treatment time and whether peroxidase treatment preceded/superceded primary antibody incubation. For each antibody, the optimal condition at Step 2 (white stars) was the starting point for Step 3. Similarly, the optimal condition for Step 3 was the starting point for Step 4. Yellow stars indicate the final automated immunohistochemistry protocol stipulated in Supplementary File x. Data in Steps 2-4 are representative of n=1-5 experiments per antibody per condition.

Fig. S2. Constitutive co-expression of necroptotic effectors is confined to fast-cycling cells within progenitors, immune and barrier populations. **A** Heatmap of cell ontologies from the *Tabula Muris* dataset (*41*). Left-most column depicts the tissue origin of each cell ontology. Other columns indicate the percent of cells within each ontology that expressed *Top2a, Mki67*, Casp8, *Ripk1, Ripk3* or *Mlkl*. Legend shows the color-to-tissue and the color-to-frequency scales. Cell ontologies of interest are annotated. **B** Micrograph of MLKL immunosignals from the wild-type mouse spleen. The white pulp (WP), marginal zone (MZ) and red pulp (RP) are annotated. Scale bar is 50µm. Scatterplot shows relative expression levels of MLKL along the white pulp-to-red pulp axis. Red datapoints show immunosignal intensities and the overlaid dark blue line indicates the LOWESS best-fit along N=20 axes from n=1 mouse. Dashed line indicates the boundary between splenic white pulp and marginal zone. Data are representative of n>3 mice. **C-D** Spatial transcriptomic data from (*46*)) and (*47*) showing the relative expression levels (arbitrary units; A.U.) of Caspase-8, RIPK1, RIPK3 or MLKL along the ileal crypt-to-villus axis (Panel C) or the hepatic central vein-to-portal vein axis (Panel D). **E-G** Spatial transcriptomic data on mouse spleen 12 days after *Plasmodium berghei*-infection. Panel E shows a Uniform Manifold Approximation and Projection (UMAP) of cell populations distinguished by unsupervised leiden clustering. Legend shows the color assigned to each population. Panel F shows the location of each cell cluster. Scale bar is 500µm. Panel G shows the normalised expression for each gene product. Expression values for *Casp8*, *Ripk1*, *Ripk3* and *Mlkl* were summated to provide an index of ‘cluster pathway expression’, which was averaged to provide an index of ‘zone pathway expression’. Data are from n=1 mouse.

Fig. S3. RIPK3 is uniquely upregulated in splenic germinal centres. A Experimental design. **B** Ki67, Caspase-8, RIPK1, RIPK3 and MLKL immunosignals from adjacent sections of the naïve or NP-KLH-immunised mouse spleen. Arrowheads show a Ki67$^+$ germinal centre that co-stains for RIPK3, but not other members of the pathway. Representative of n>3 mice per group. Scale bars in lower magnification micrographs are 500µm. Scale bars in insets are 100µm. **C-H** Ripk3-/-, +/- or +/+ mice were immunised with NP-KLH and 14 days later the circulating white blood cell count (Panel C), splenic mature B cells (Panel D), splenic NP-specific IgG1+ cells (Panel E), splenic NP-specific IgG1+ CD138+ cells (panel F), low affinity NP-specific antibody (Panel G) and high affinity NP-specific antibody (Panel H) were measured. Each datapoint represents one mouse. *p<0.05 by two-sided t-test with Welch's correction.

Fig. S4. Standardised quality control and optimisation of the immunohistochemical detection of human necroptotic proteins. Summary of the optimisation for immunodetection with monoclonal antibodies against human MLKL, RIPK3, RIPK1, Caspase-8 and Caspase-10 (C10). Step 1: Immunoblot signals for each antibody on lysates from wild-type (WT) versus *MLKL*$^{-/-}$ or *RIPK1*$^{-/-}$ or *CASP8*$^{-/-}$*CASP10*$^{-/-}$*MLKL*$^{-/-}$ (KO) HT29 cells after treatment with the indicated stimuli. Arrowheads indicate the full-length protein of interest. Representative GAPDH immunoblots are shown as loading controls. Data are representative of n=1-2 immunoblots per antibody. Steps 2-4: Heatmaps depict the integrated signal-to-noise values derived from immunohistochemical signals for each antibody on WT versus KO HT29 cells. Legend shows the heatmap colour-to-value scale. Step 2 varied the primary antibody concentration and the antigen retrieval pH. Step 3 varied the blocking reagent and the antigen retrieval time. Step 4 varied the amplification technique, amplification time, peroxidase treatment time and whether peroxidase treatment preceded/superceded primary antibody incubation. For each antibody, the optimal condition at Step 2 (white stars) was the starting point for Step 3. Similarly, the optimal condition for Step 3 was the starting point for Step 4. Yellow stars indicate the final automated immunohistochemistry protocol stipulated in Supplementary File x. Data in Steps 2-4 are representative of n=1-5 experiments per antibody per condition. The annotation 'see Fig. S1' indicates optimisations that were only done using mouse tissues because these antibodies recognise both human and mouse orthologs.

Fig. S5. Automated immunohistochemistry to detect necroptotic signaling in mouse cells. Immunosignals of cleaved Caspase-3, Caspase-8, RIPK1, RIPK3 and MLKL in wild-type mouse dermal fibroblasts. Arrowheads indicate Caspase-8$^+$, RIPK1$^+$ puncta that are presumed to be necrosomes. Data are representative of n=1 for each protein and treatment. Scale bars in lower magnification micrographs are 10µm. Scale bars in insets are 1µm.

Table S1. Patient and clinical data related to **Fig. 6**.


A
Quantitation of IHC specificity
i)
pixel count (x10^5)
5
4
3
2
1
0
KO
WT
WT
KO
ii)
S/N ratio
600
400
200
0
integration of S/N
iii)
1.5E+06
0
50
100
150
200
250
Signal intensity
B
IHC signal-to-noise values
C8 D35G2
C8 1G12
C8 3B10
R1 D94C12
R3 8G7
R3 1H12
MLKL 5A6
ileum
colon
liver
spleen
kidney
heart
brain
low amount of specific signal
high amount of specific signal
C
protein abundance
C8
R1
R3
MLKL
sm. int.
colon
liver
spleen
kidney
heart
brain
below detection
max
D
Caspase-8
RIPK1
RIPK3
MLKL
ileum
colon
liver
spleen
kidney
heart
brain
WT
KO


A
zones
Caspase-8
RIPK1
RIPK3
i) ileum
tip
crypt
ii) colon
tip
crypt
iii) liver
BD
CV
PV
iv) spleen
WP
MZ
CA
RP
B
C8 RIP1 RIP3 MLKL
Caspase-8
RIPK1
RIPK3
ileum
crypt
tip
colon
crypt
tip
liver
CV
spleen
WP
MZ
RP
IHC signal (A.U.)
relative distance
0.00 0.25 0.50 0.75 1.00
3B10
micron
0 50 100 150 200
C
r=0.98
r=0.35
r=0.83
Top2a + (%)
Mki67 + (%)
Ripk1 + (%)
Ripk3 + (%)
1 2.5 10 25 100

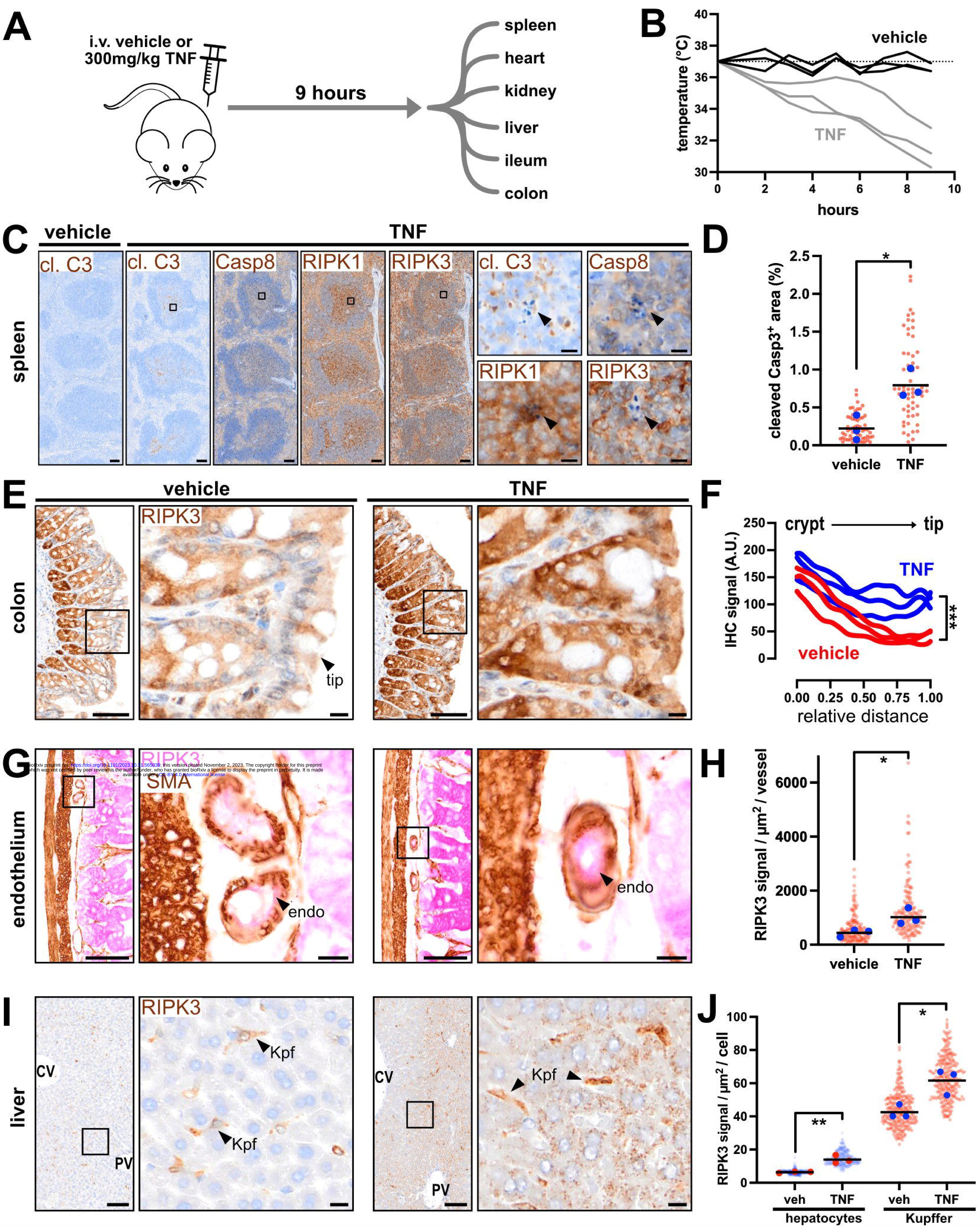
A
i.v. vehicle or
300mg/kg TNF
9 hours
spleen
heart
kidney
liver
ileum
colon
B
temperature (°C)
40
38
36
34
32
30
0
2
4
6
8
10
hours
vehicle
TNF
C
vehicle
TNF
spleen
cl. C3
cl. C3
Casp8
RIPK1
RIPK3
cl. C3
Casp8
RIPK1
RIPK3
D
cleaved Casp3⁺ area (%)
2.5
2.0
1.5
1.0
0.5
0.0
*
vehicle
TNF
E
vehicle
TNF
colon
RIPK3
tip
F
IHC signal (A.U.)
250
200
150
100
50
0
crypt
tip
TNF
vehicle
***
0.00
0.25
0.50
0.75
1.00
relative distance
G
endothelium
RIPK3
SMA
endo
endo
H
RIPK3 signal / µm² / vessel
6000
4000
2000
0
*
vehicle
TNF
I
liver
RIPK3
CV
PV
Kpf
Kpf
CV
PV
Kpf
J
RIPK3 signal / µm² / cell
100
80
60
40
20
0
**
*
veh
TNF
veh
TNF
hepatocytes
Kupffer


A
p.o. water
or antibiotics
6 days
spleen
ileum
colon
B
antibiotics
Mlkl
Ripk3
Casp8
Lyz1
Reg3b
Ripk1
ileum
–
+
spleen
–
+
2
1
0
-1
-2
C
ileum
spleen
antibiotics
–
+
–
+
Lysozyme
20
15
RIPK3
75
50
35
25
20
RIPK1
100
75
50
35
25
Caspase-8
75
50
35
25
20
Coomassie
D
Caspase-8
RIPK1
RIPK3
water
antibiotics


A
cl. Caspase-3
Caspase-8
RIPK1
MLKL
WT
KO
untreated
TNF alone
TNF-induced apoptosis (TS)
TNF-induced necroptosis (TSI)
B
cells with puncta (% of total)
0
10
20
30
40
Legend
untreated
TNF
TS
TSI
TSI (KO)
C
puncta per cell
0
2
4
6
8
10
12
****
Caspase-8
clone B.925.8
Caspase-8
clone D35G2
RIPK1
clone D94C12
MLKL
clone EPR17514


A
non-IBD or IBD patient
intestine biopsies collected
clinical indices
immunoblot
IHC
B
non-IBD
IBD
non-infl
margin
inflamed
RHI score
0
4
8
12
16
Legend
Patient A
Patient B
Patient C
Patient D
Patient E
Patient F
Patient G
Patient H
C
control cell lysates
apoptosis in UC
necroptosis in UC
apoptosis in CD
necroptosis in CD
patient biopsies
R3-/- or MLKL-/- +TSI
RIPK1-/- +TSI
WT +TSI
WT TS
WT untreated
IBD inflamed
IBD margin
IBD non-inflamed
non-IBD
blank
pMLKL
MLKL
pRIPK3
RIPK3
pRIPK1
RIPK1
Caspase-10
Caspase-8
Caspase-3
GAPDH
A B B B
C D D D
E F F
G H H H
study ID
D
non-IBD (patient C)
IBD (patient D)
non-inflamed
inflamed
a b c d e f g h i j k l m n o
E
**
ns
ns
necrosomes per 100 cells
0
20
40
60
80
100
non-IBD (patient C)
non-inflamed (patient D)
inflamed (patient D)